Supplement of Geosci. Model Dev., 14, 5789–5823, 2021
https://doi.org/10.5194/gmd-14-5789-2021-supplement

Geoscientific Model Development
Open Access
EGU

Supplement of

GCAP 2.0: a global 3-D chemical-transport model framework for past, present, and future climate scenarios

Lee T. Murray et al.

Correspondence to: Lee T. Murray (lee.murray@rochester.edu)

Contents

S1 Meteorology

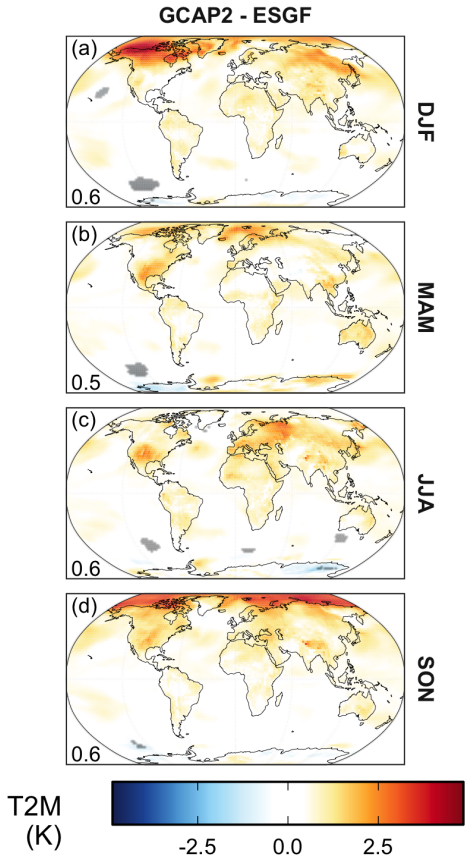

Figure S1: Difference in seasonal mean surface temperature (in K) in our repeat simulation with respect to the original r1i1p1f2 variant. Rows from top to bottom show the 14-year seasonal average for 2001-2014 C.E. for December-January-February (DJF), March-April-May (MAM), June-July-August (JJA), and September-October-November (SON). Gray dots indicate locations where the E2.1 simulations are statistically different with respect to interannual variability (p-value < 0.05; $n = 14$ yr). The number in the bottom left gives the global mean value.

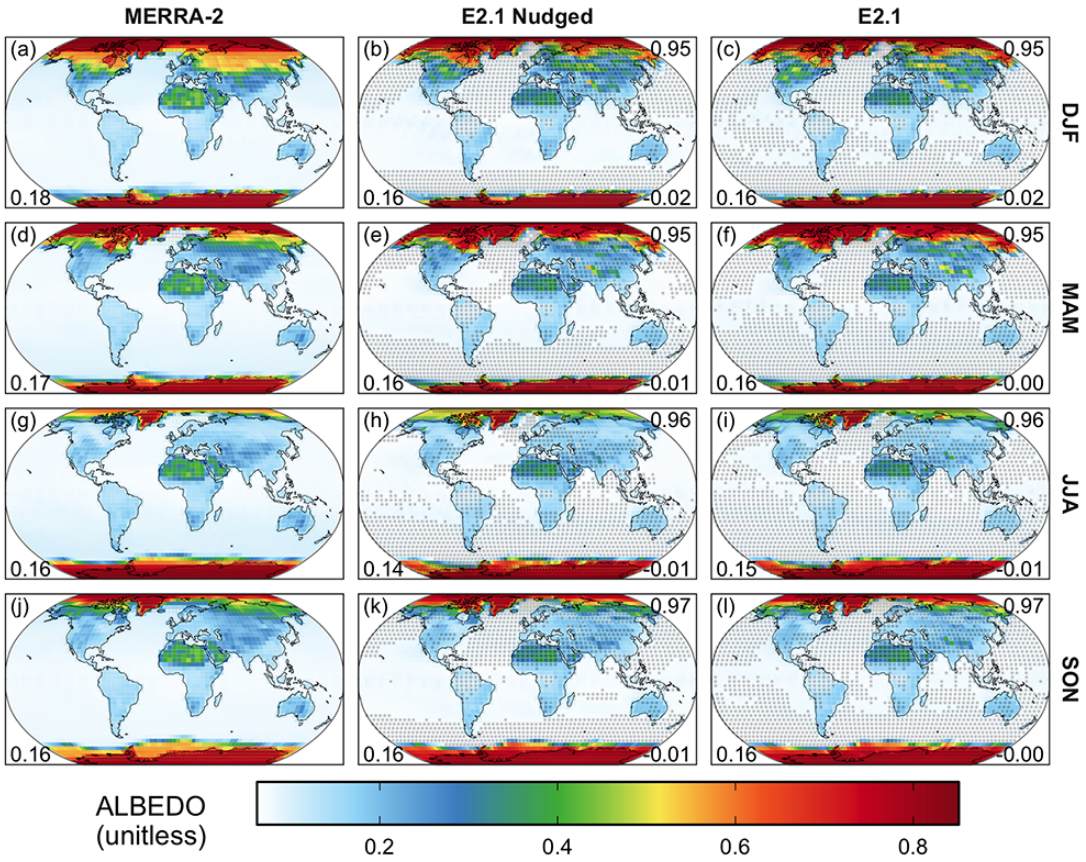

Figure S2: Seasonal mean climatology of the surface broadband albedo (unitless; variable name: ALBEDO). Rows from top to bottom show the 10-year seasonal average for 2005-2014 C.E. for December-January-February (DJF), March-April-May (MAM), June-July-August (JJA), and September-October-November (SON). Columns from left to right show the values from the MERRA-2 reanalysis (Gelaro et al., 2017), E2.1 nudged to MERRA-2, and the free-running E2.1. All products have been horizontally re-gridded to a common 4° latitude by 5° longitude resolution for comparison. Gray dots indicate locations where the E2.1 simulations are statistically different with respect to interannual variability (p-value < 0.05; $n = 10$ yr). The number in the bottom left gives the global mean value. The number in the top right of the E2.1 panels gives the pattern correlation (R) between the E2.1 runs and MERRA-2. The number in the bottom right of the E2.1 panels gives the mean difference of the simulation with respect to its MERRA-2 equivalent.

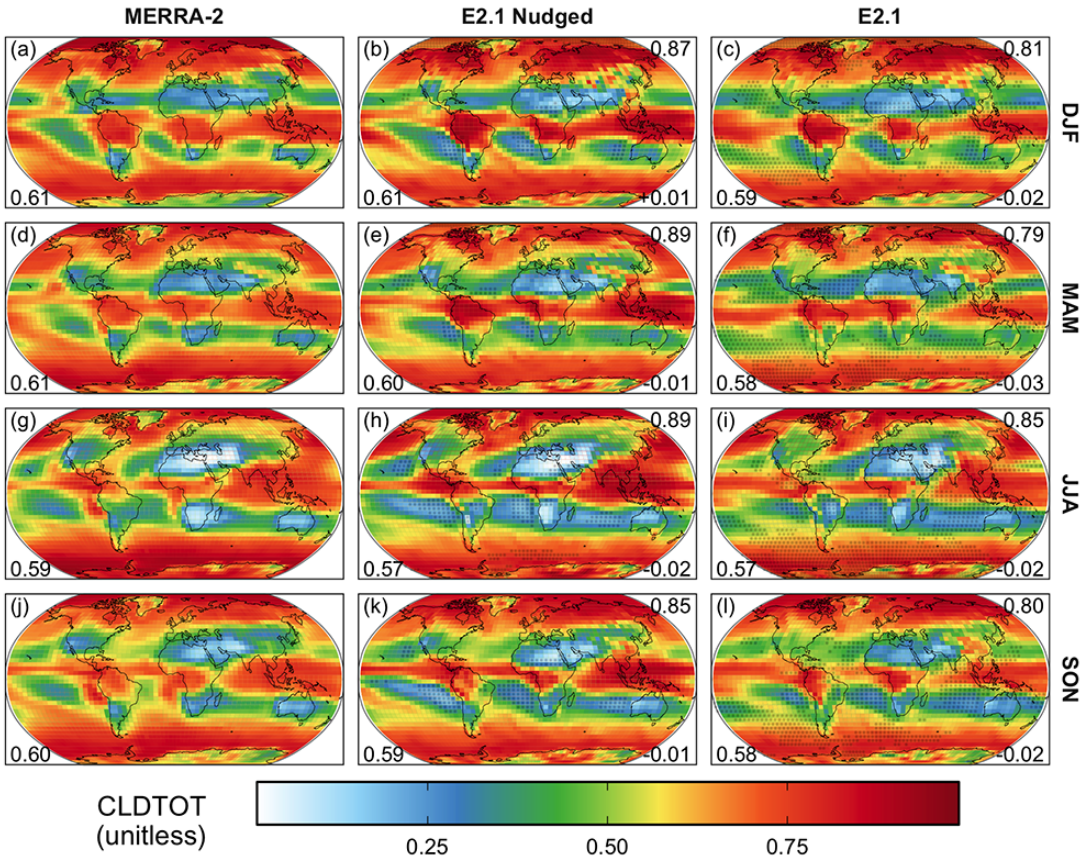

Figure S3: The same as Fig. S2, but for total cloud area fraction (unitless; variable name: CLDTOT).

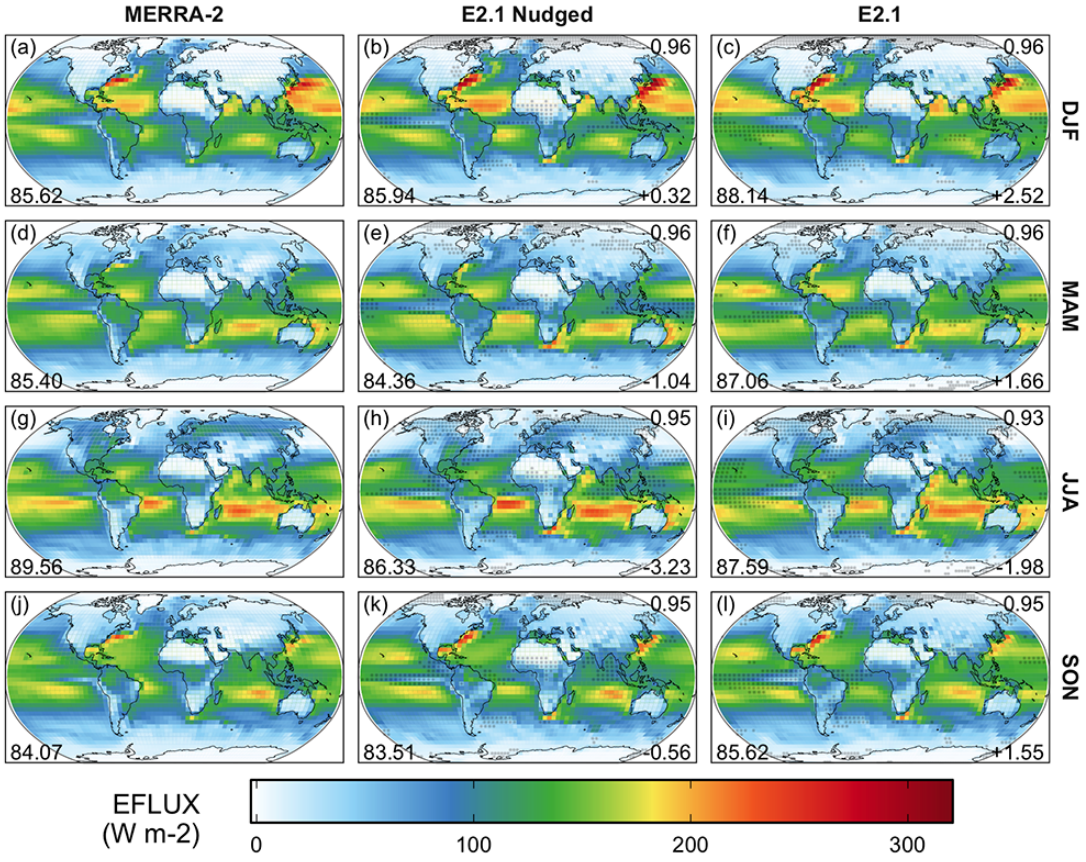

Figure S4: The same as Fig. S2, but for total latent energy flux (units: W m^{-2}; variable name: EFLUX).

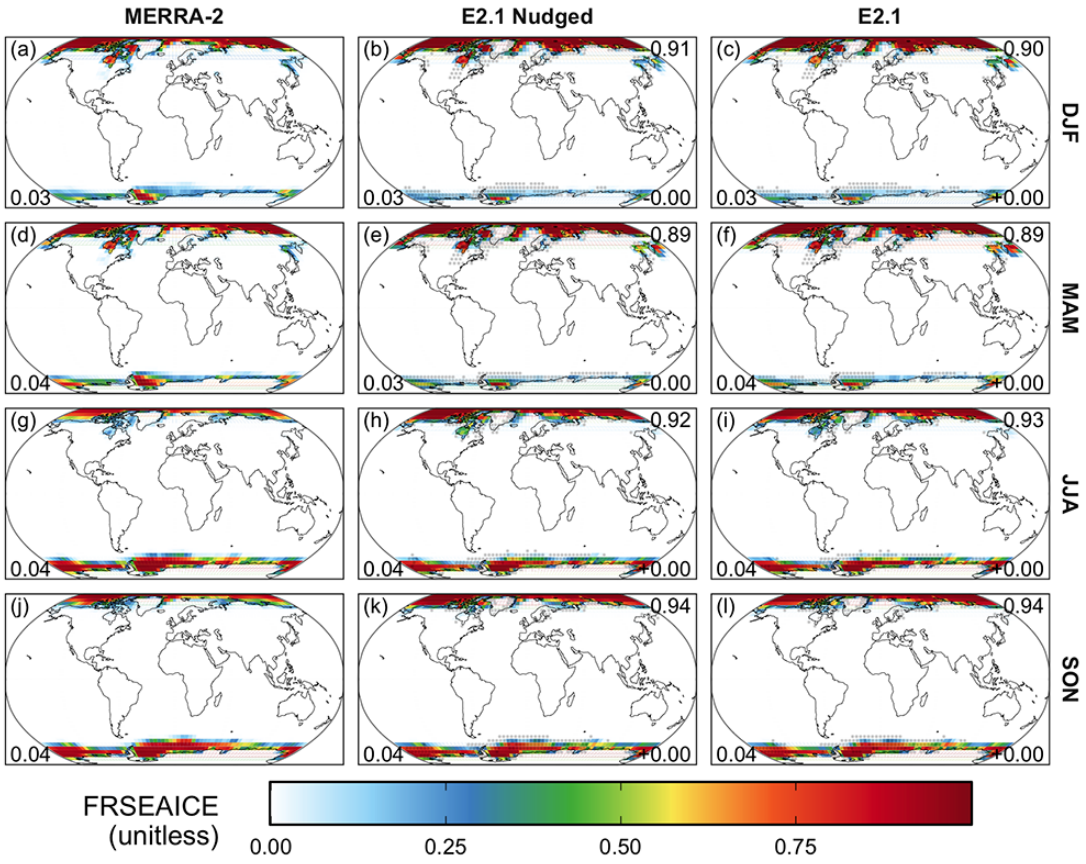

Figure S5: The same as Fig. S2, but for fraction of sea ice (unitless; variable name: FRSEAICE).

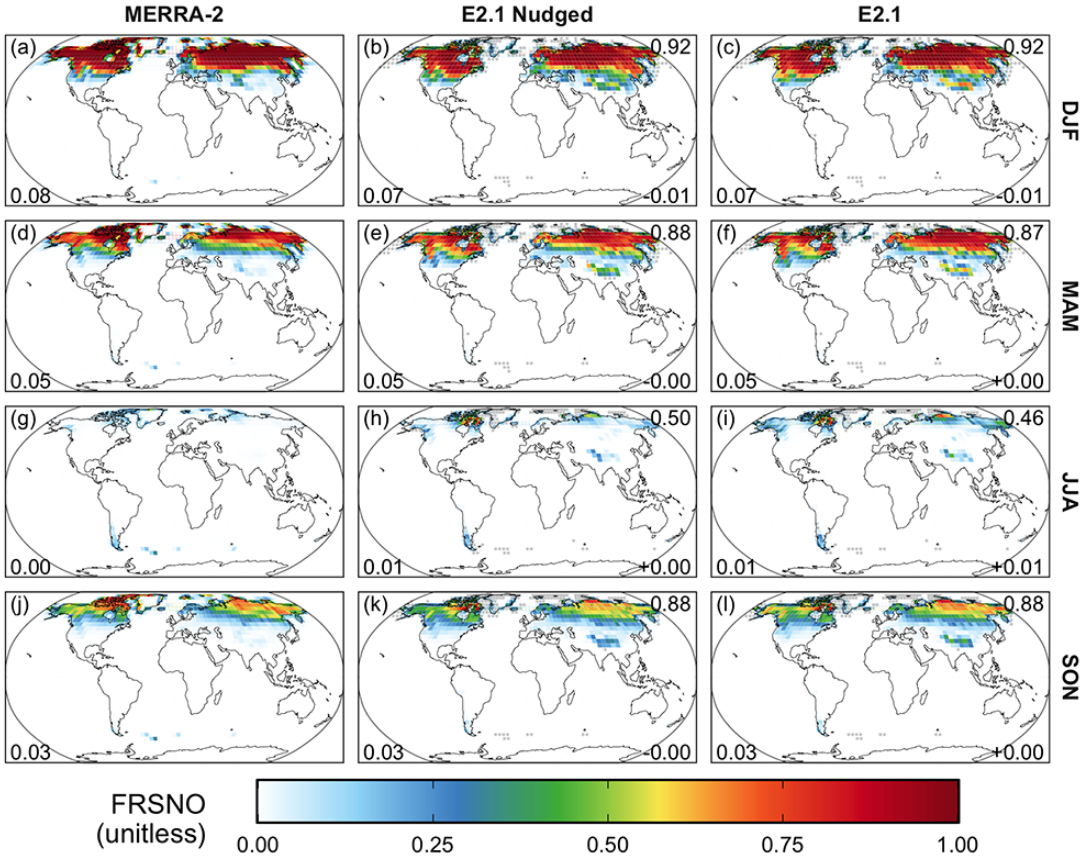

Figure S6: The same as Fig. S2, but for fraction of snow coverage on land (unitless; variable name: FRSNO).

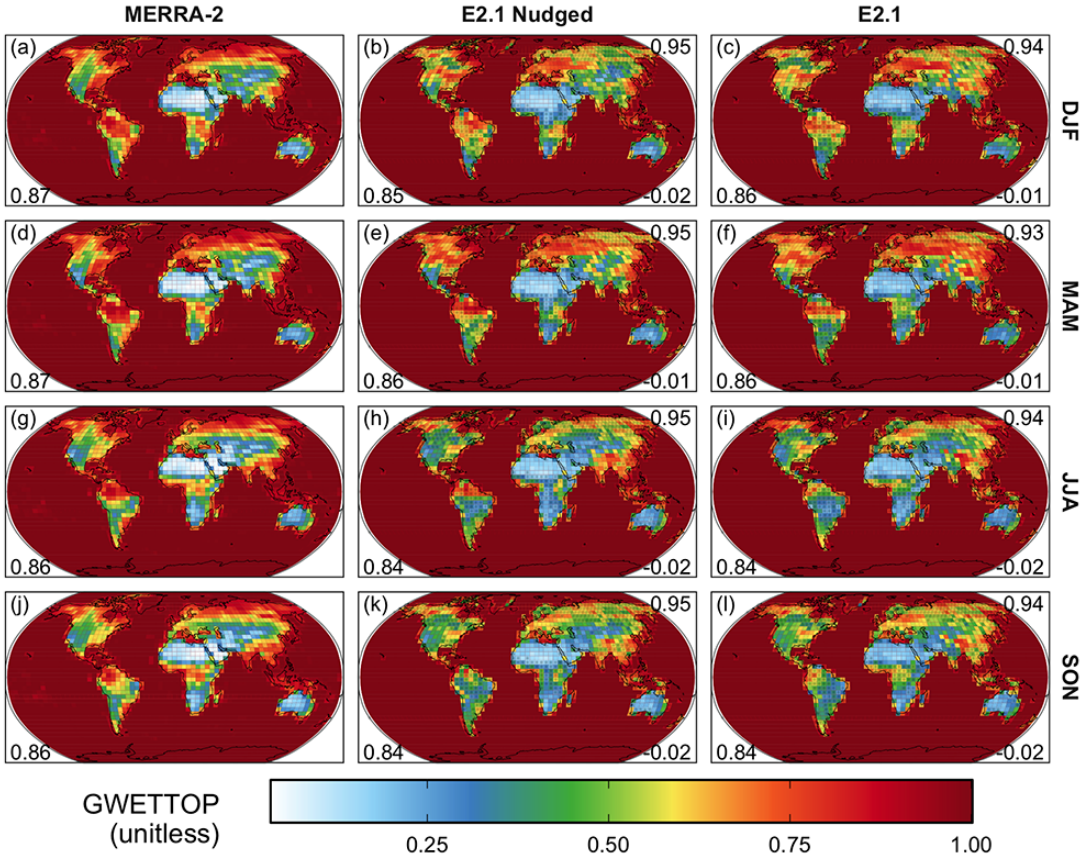

Figure S7: The same as Fig. S2, but for surface soil wetness (unitless; variable name: GWETTOP).

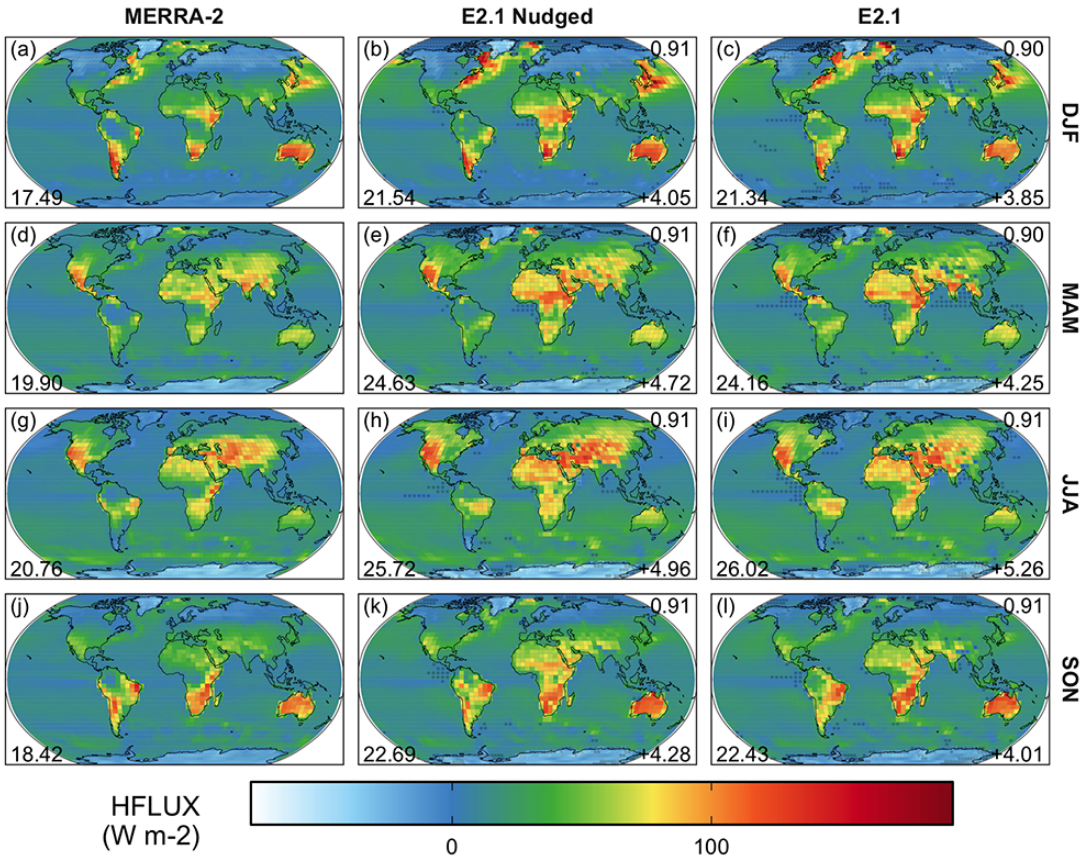

Figure S8: The same as Fig. S2, but for surface sensible heat flux from turbulence (units: W m^{-2}; variable name: HFLUX).

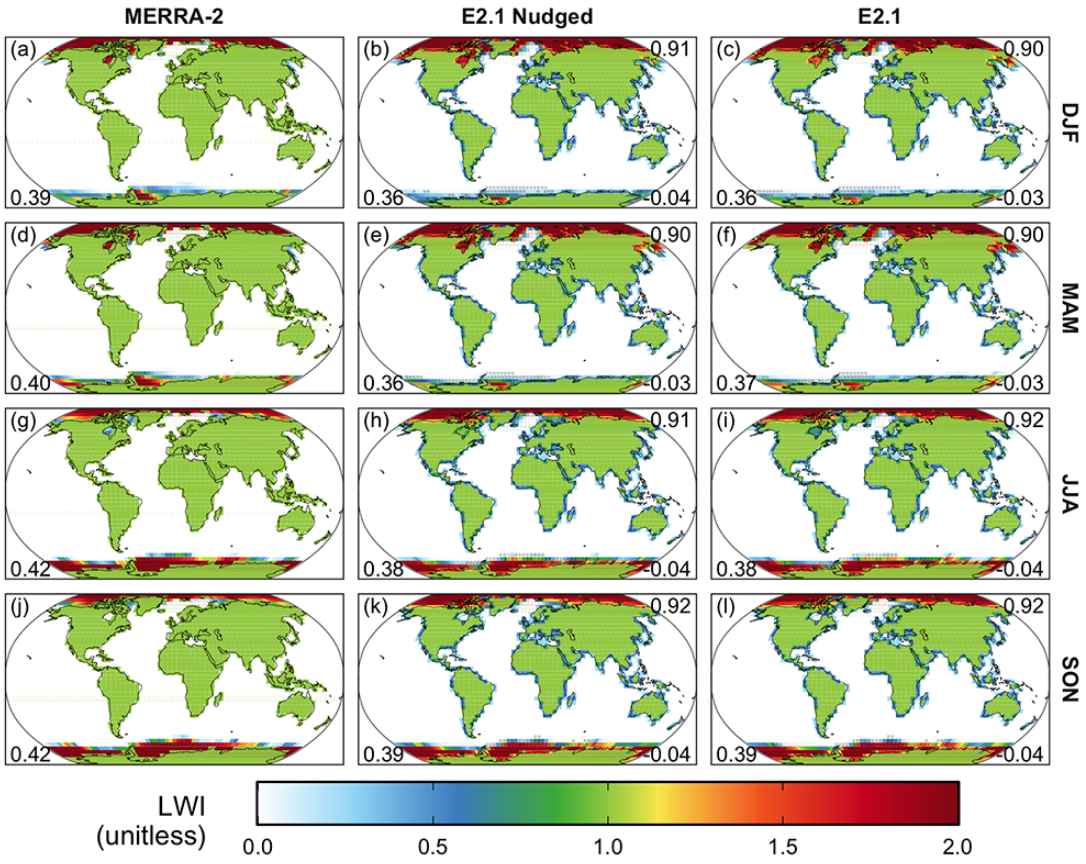

Figure S9: The same as Fig. S2, but for water (0), land (1), or ice (2) surface classification (unitless; variable name: LWI).

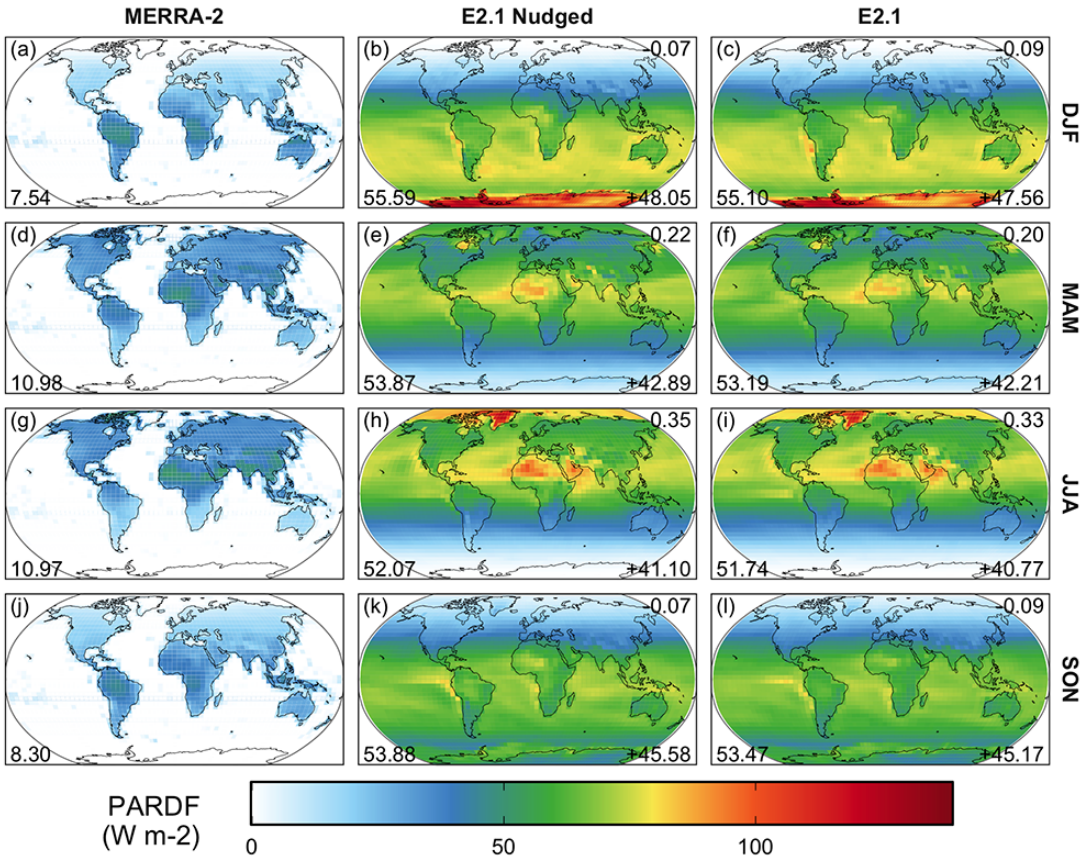

Figure S10: The same as Fig. S2, but for photosynthetically active diffuse downward radiation (units: W m^{-2}; variable name: PARDF).

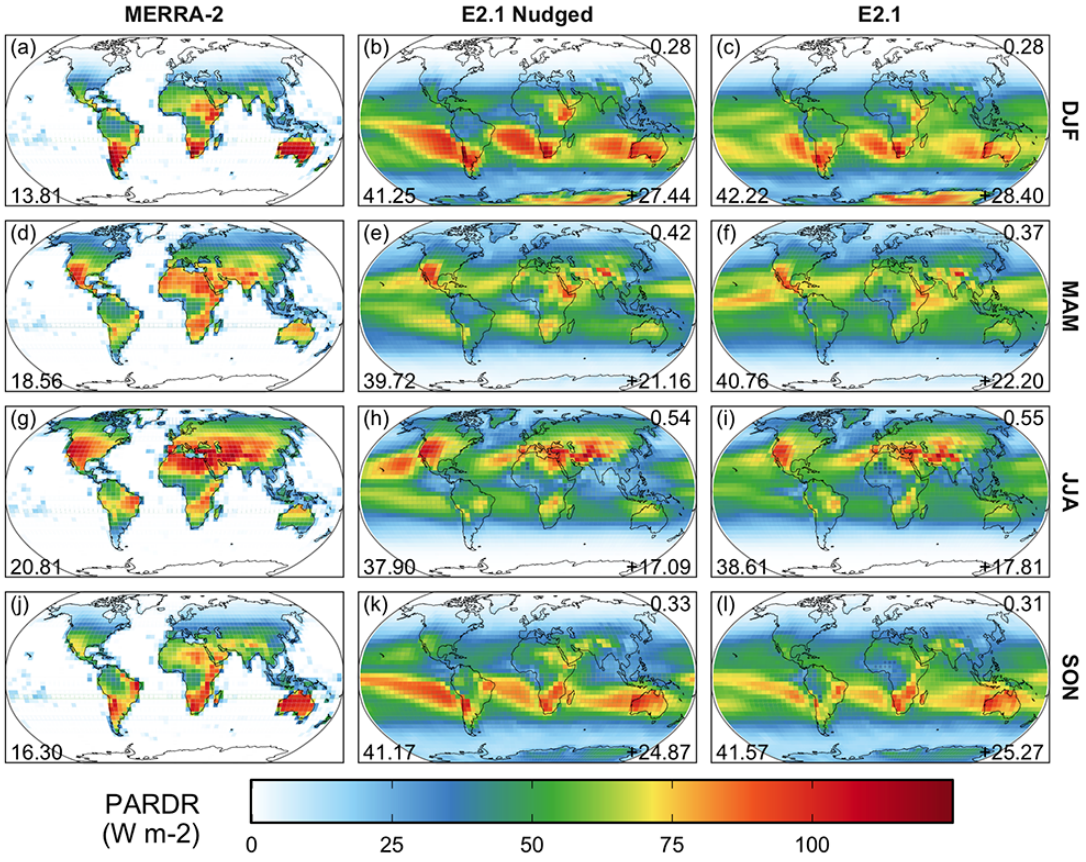

Figure S11: The same as Fig. S2, but for photosynthetically active direct downward radiation (units: W m^{-2}; variable name: PARDR).

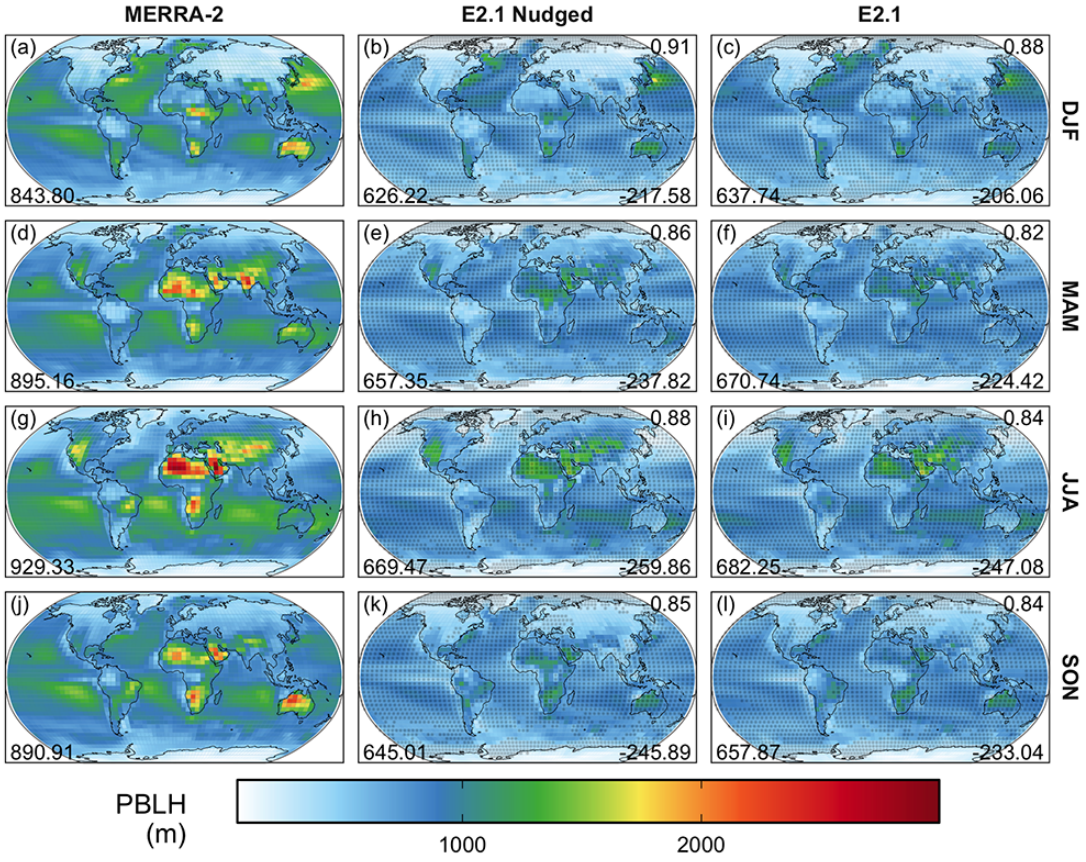

Figure S12: The same as Fig. S2, but for planetary boundary layer height (units: m; variable name: PBLH).

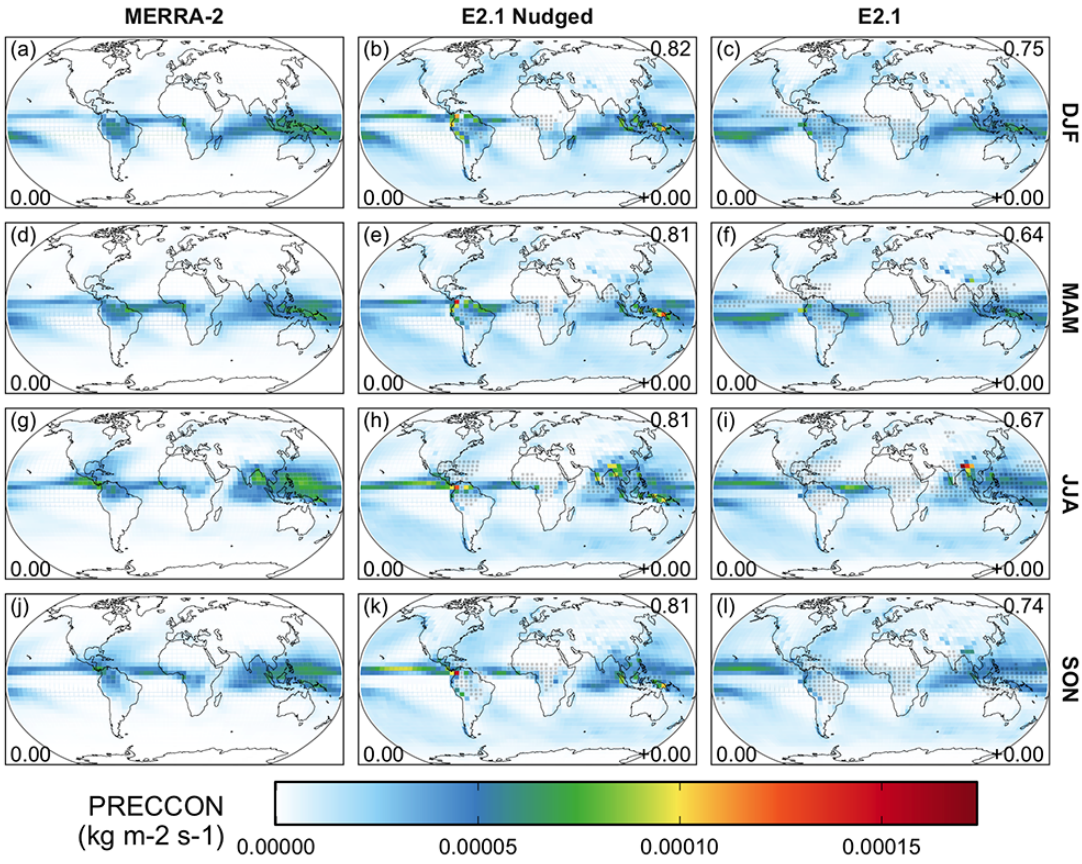

Figure S13: The same as Fig. S2, but for convective precipitation (units: kg m^{-2} s^{-1}; variable name: PRECCON).

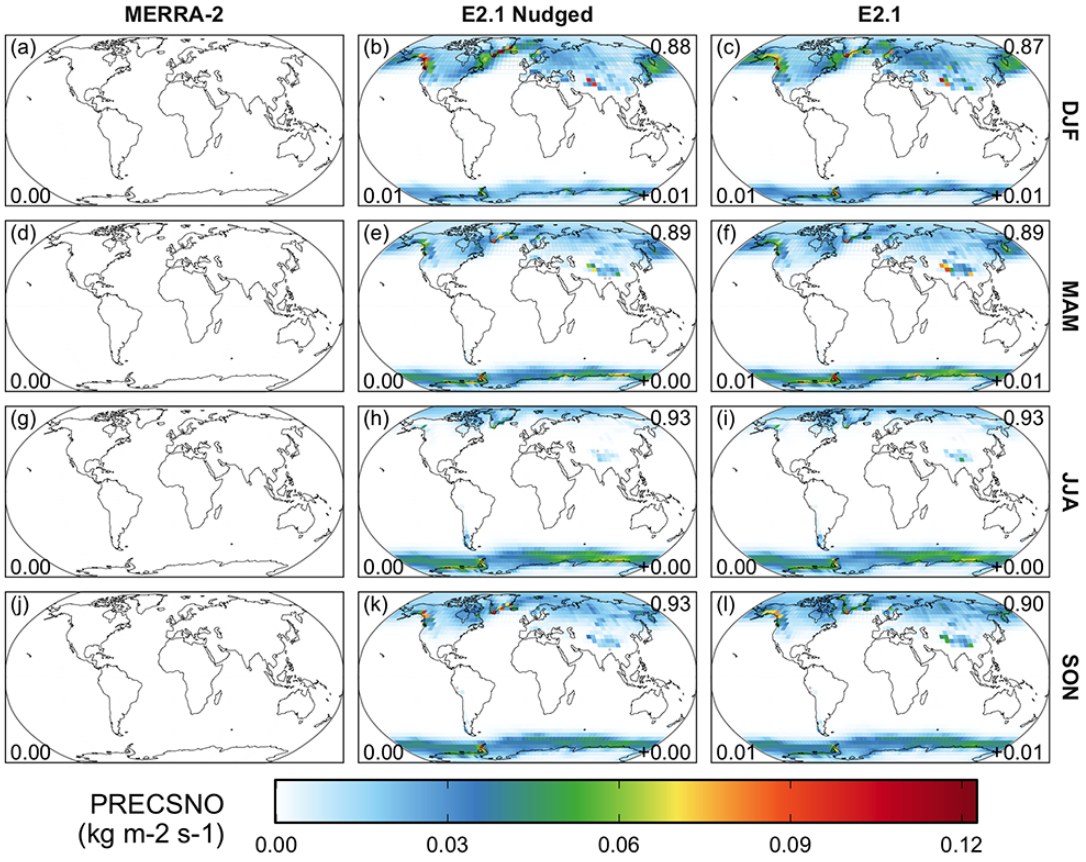

Figure S14: The same as Fig. S2, but for snow precipitation (units: kg m^{-2} s^{-1}; variable name: PRECSNO).

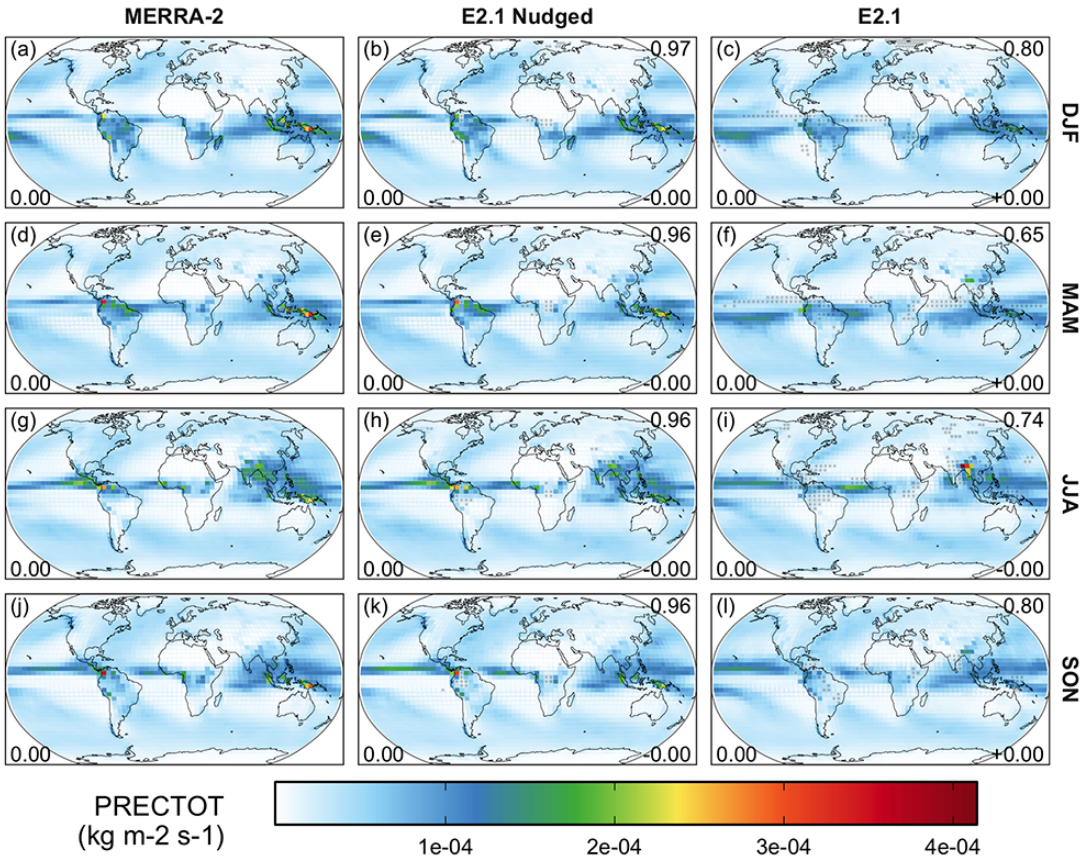

Figure S15: The same as Fig. S2, but for total precipitation (units: kg m^{-2} s^{-1}; variable name: PRECTOT).

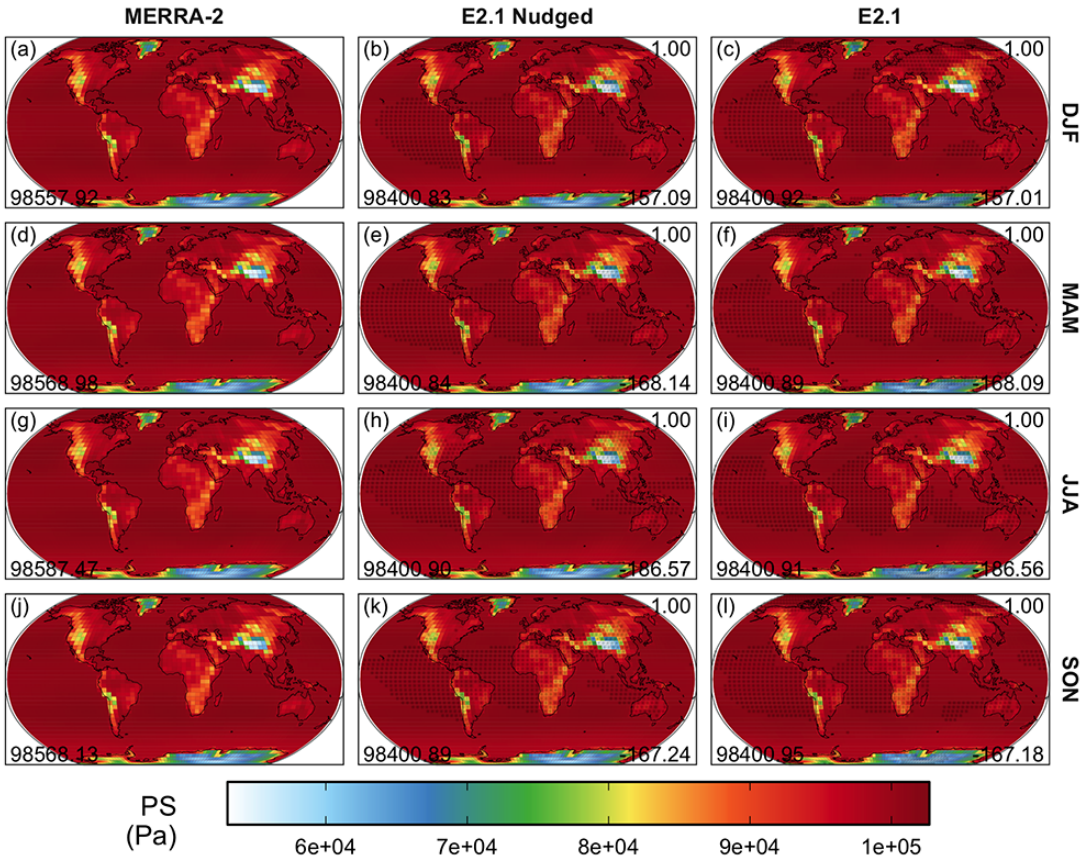

Figure S16: The same as Fig. S2, but for surface pressure (units: Pa; variable name: PS).

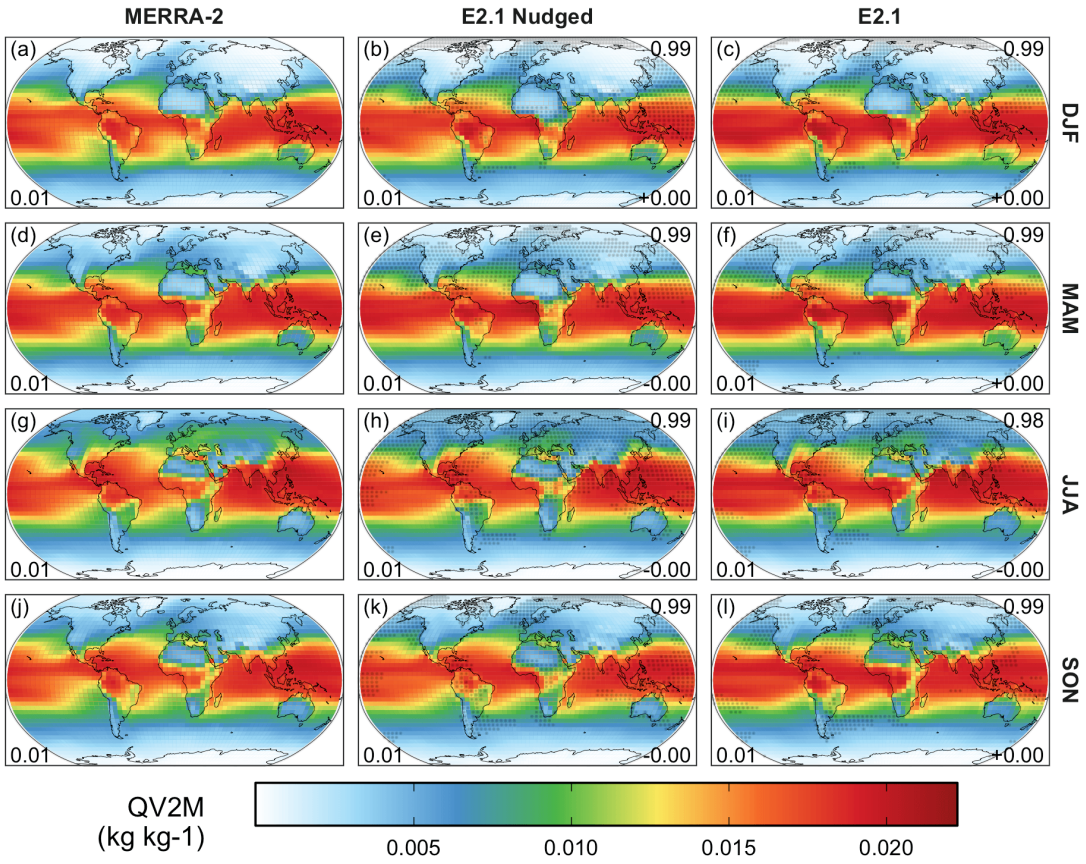

Figure S17: The same as Fig. S2, but for specific humidity at 2 m above the surface (units: kg kg^{-1}; variable name: QV2M).

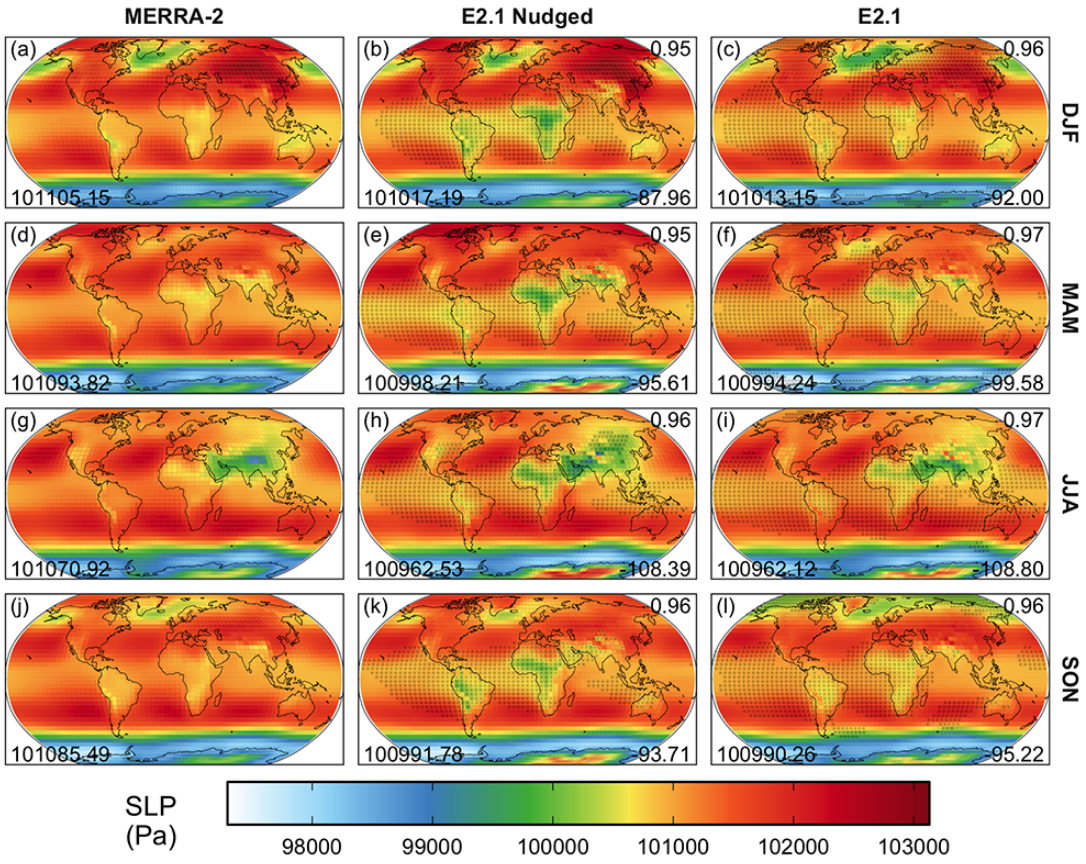

Figure S18: The same as Fig. S2, but for sea-level pressure (units: Pa; variable name: SLP).

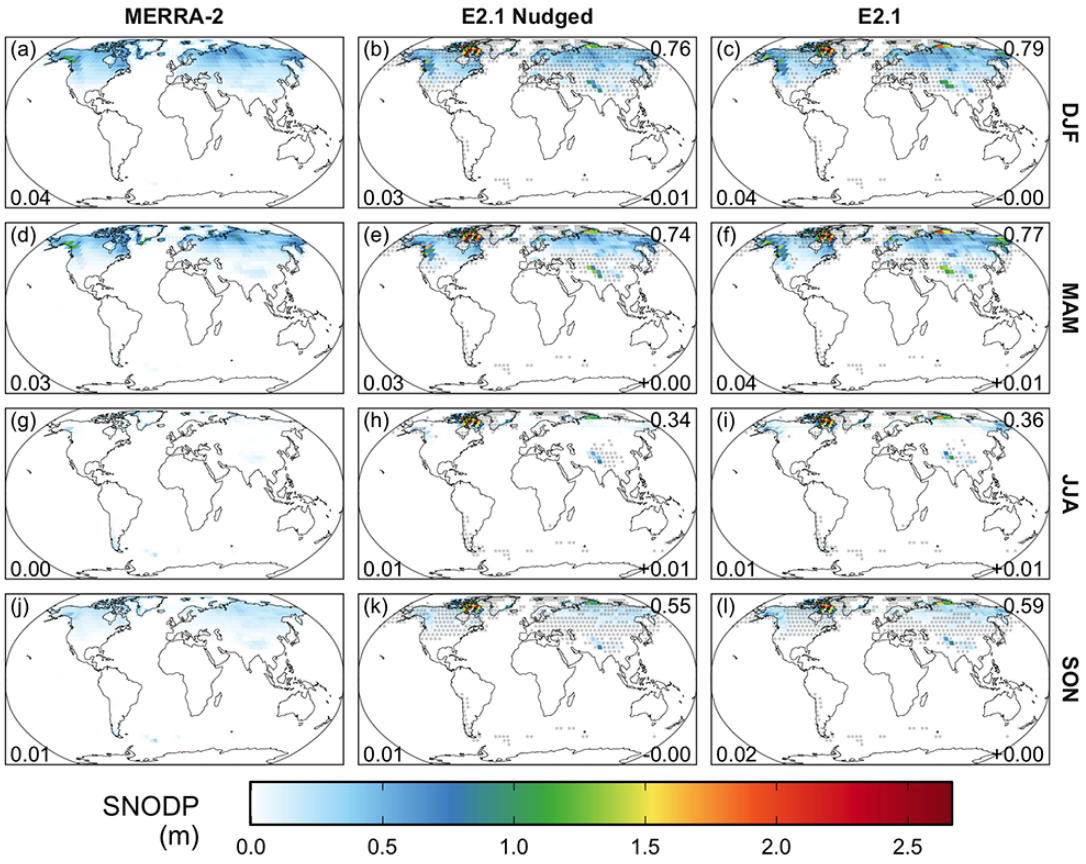

Figure S19: The same as Fig. S2, but for snow depth (units: m; variable name: SNODP).

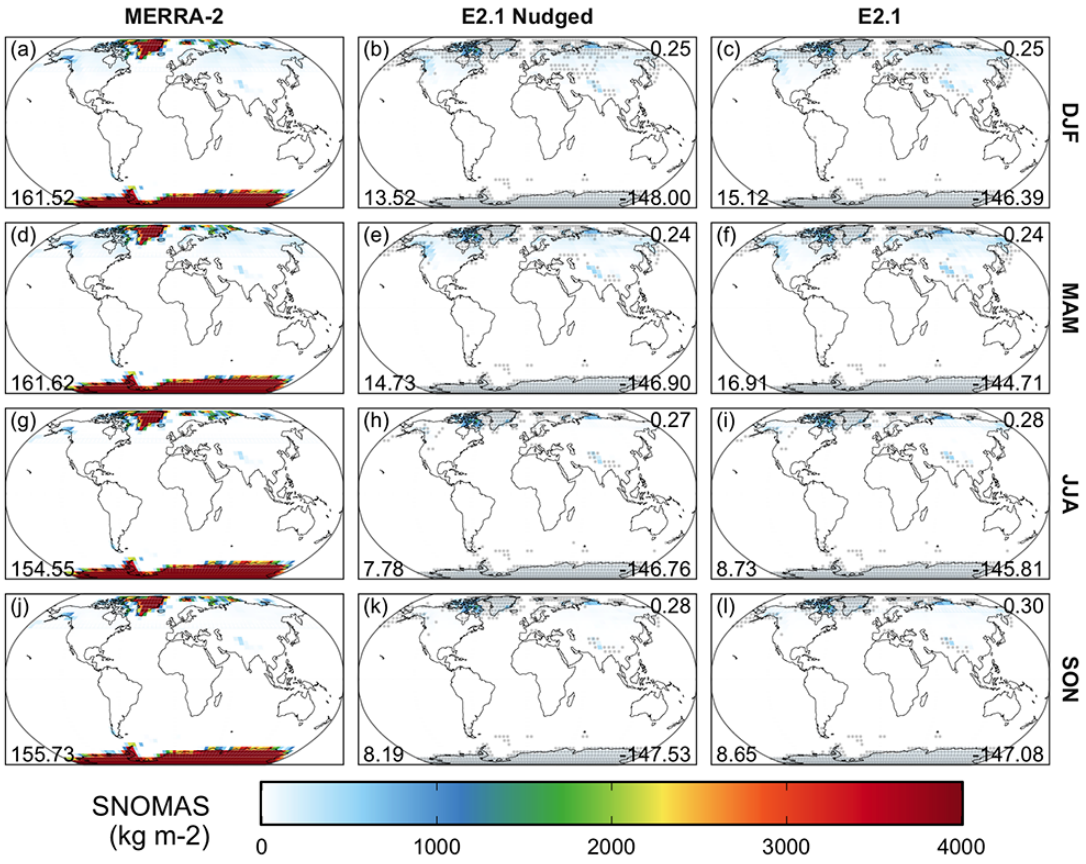

Figure S20: The same as Fig. S2, but for total snow storage on land (units: m; variable name: SNOMAS).

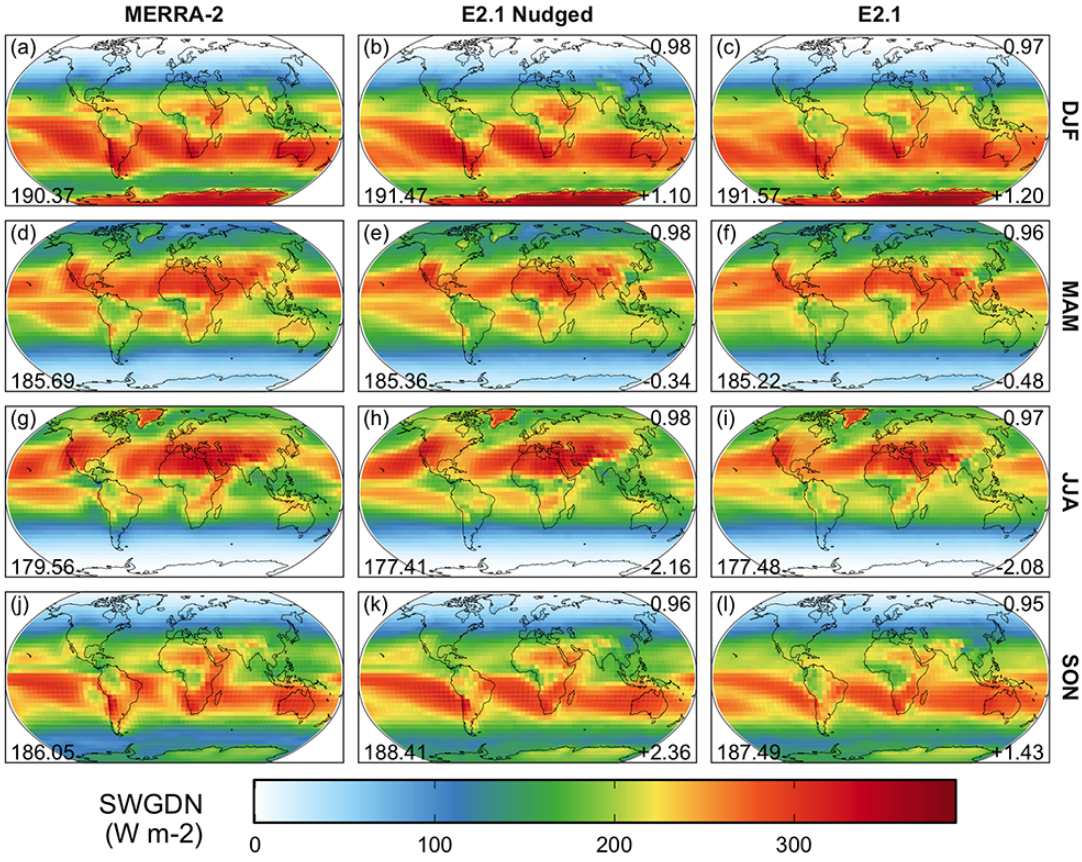

Figure S21: The same as Fig. S2, but for downwelling shortwave flux at the surface (units: W m^{-2}; variable name: SWGDN).

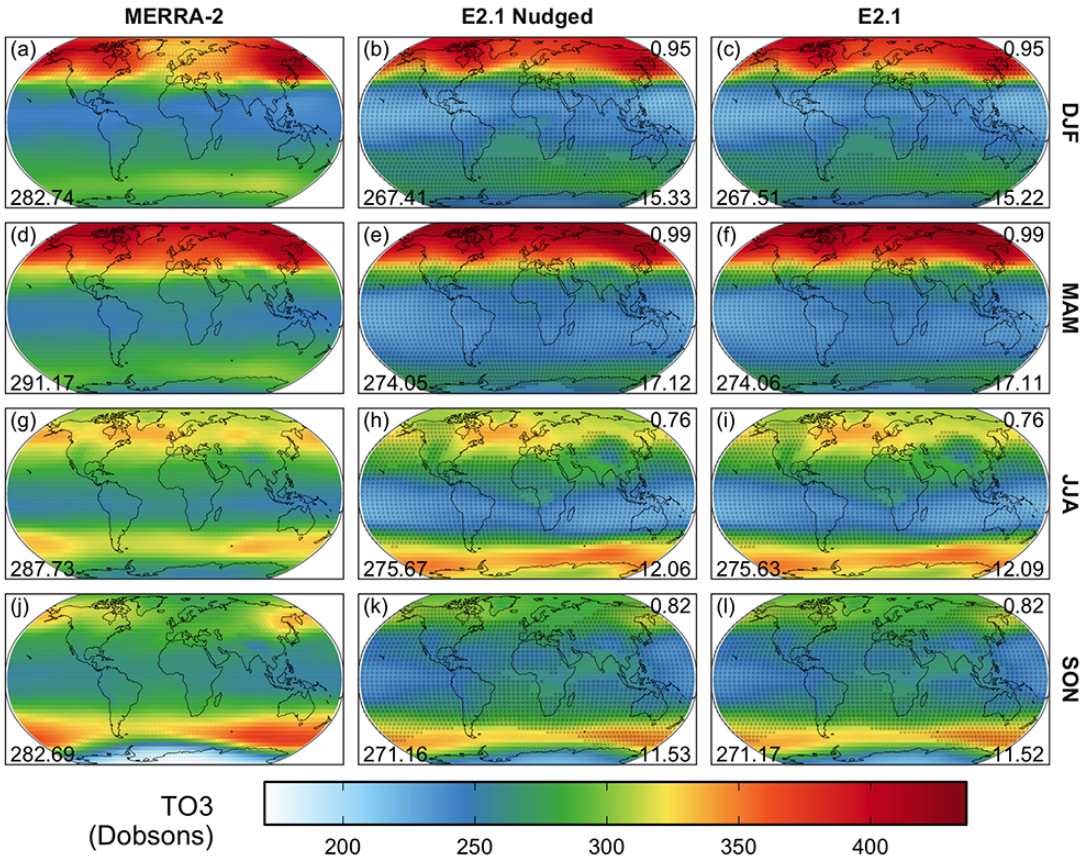

Figure S22: The same as Fig. S2, but for total ozone column used in the general circulation model (units: Dobson Units; variable name: TO3).

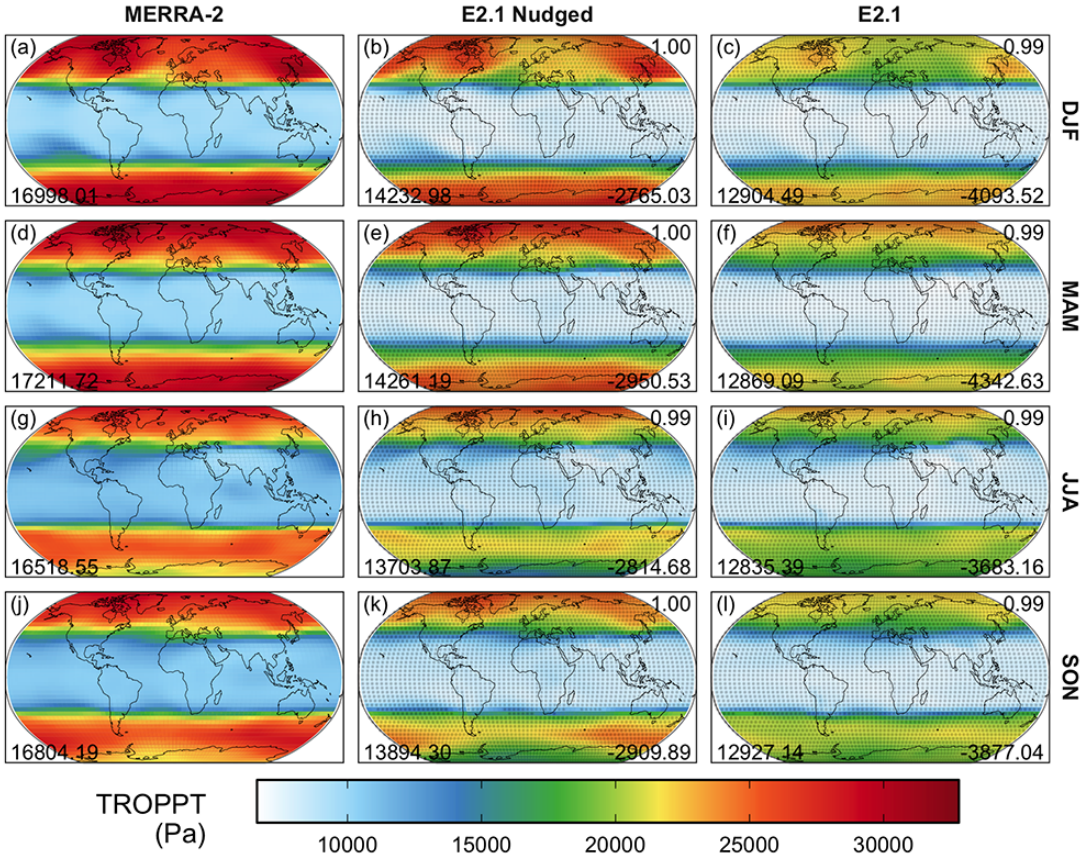

Figure S23: The same as Fig. S2, but for tropopause pressure (units: Pa; variable name: TROPPT).

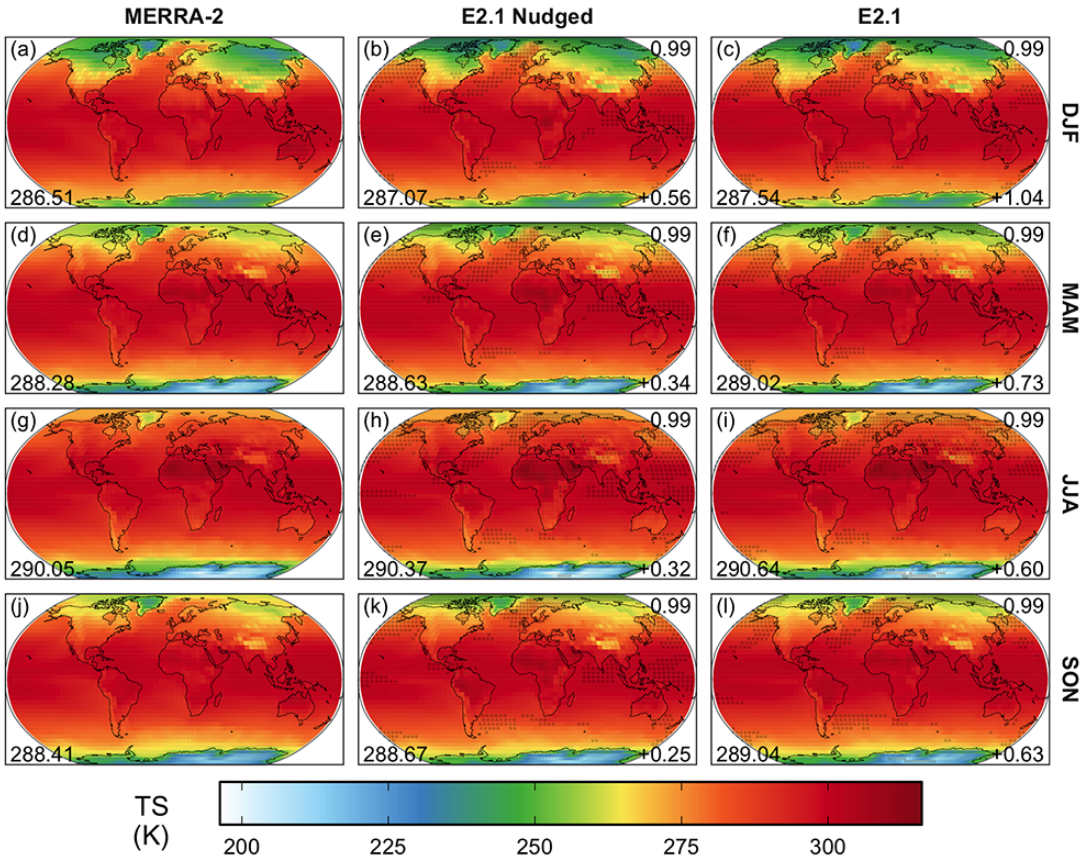

Figure S24: The same as Fig. S2, but for the surface skin (land- and sea-surface) temperature (units: K; variable name: TS).

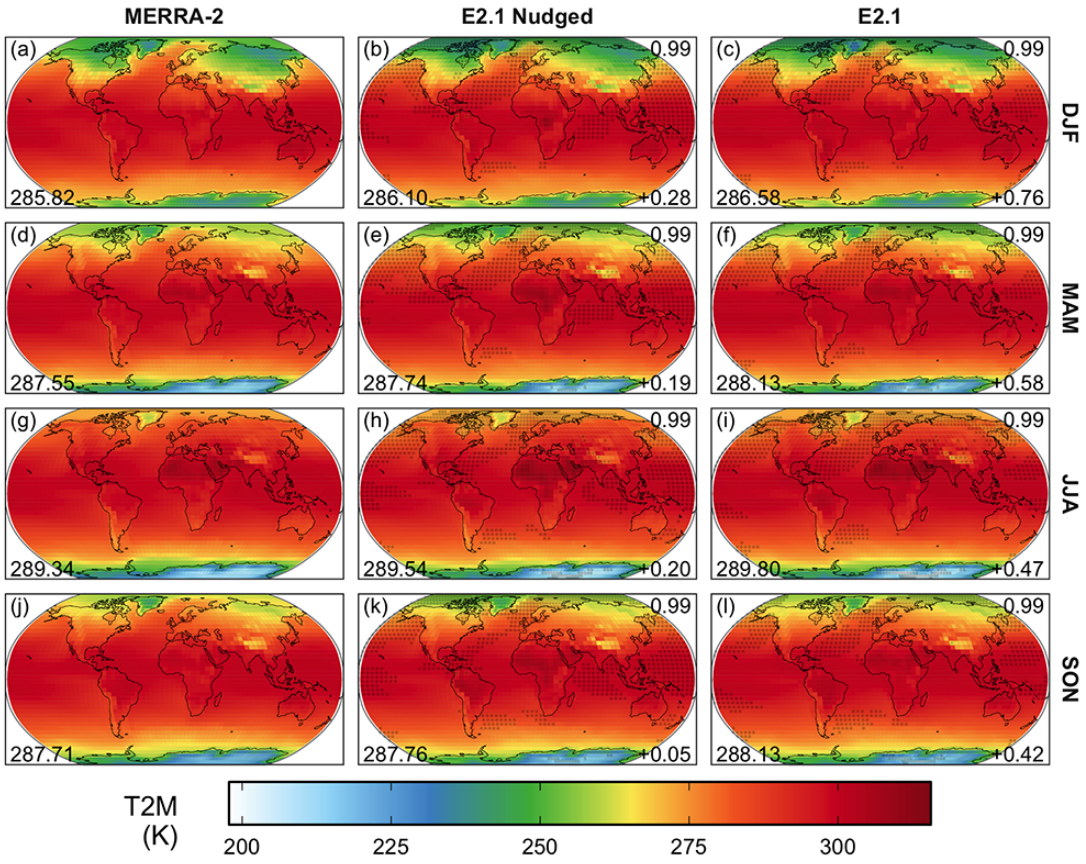

Figure S25: The same as Fig. S2, but for the atmospheric temperature at 2 m above the surface (units: K; variable name: T2M).

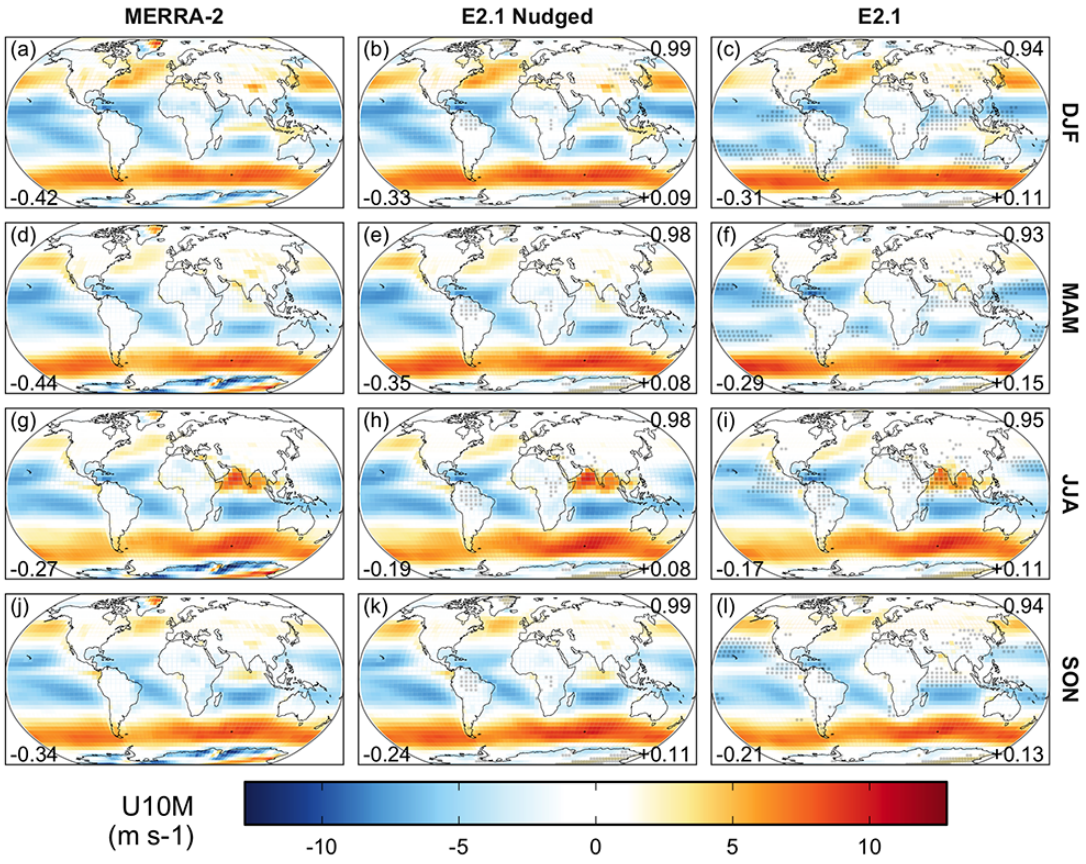

Figure S26: The same as Fig. S2, but for the zonal wind component at 10 m above the surface (units: m s^{-1}; variable name: U10M).

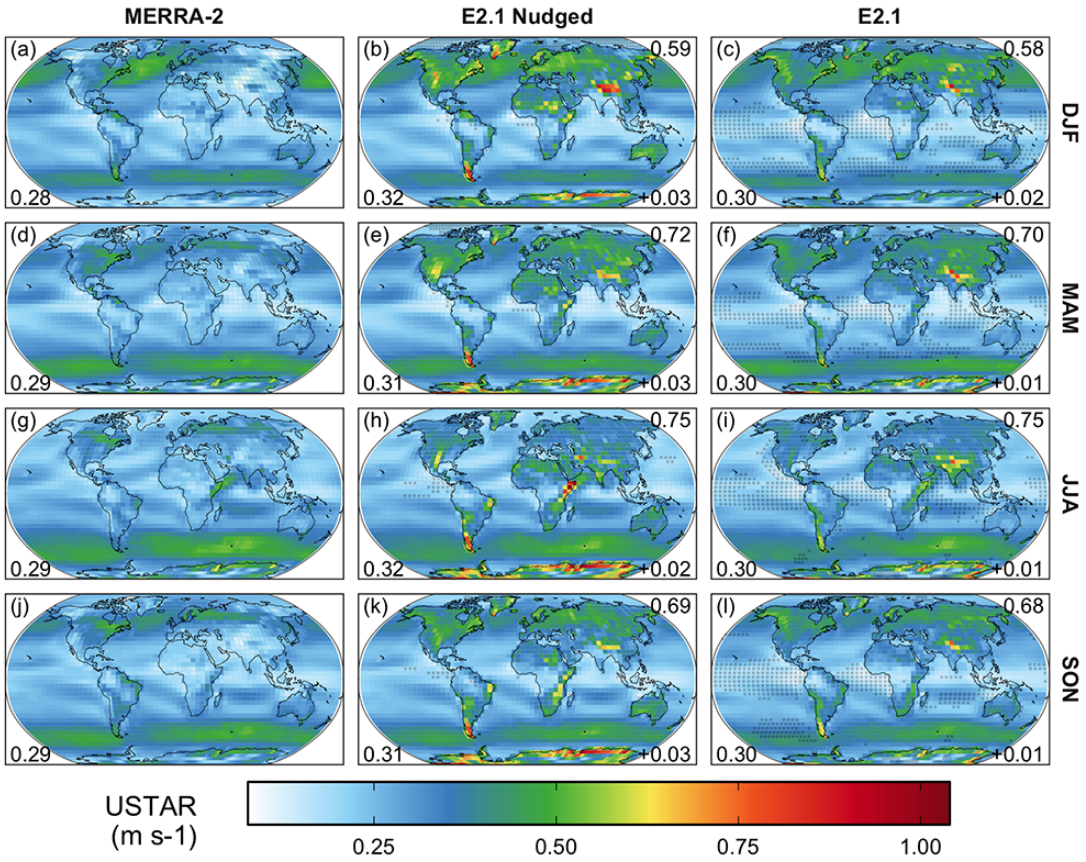

Figure S27: The same as Fig. S2, but for the surface friction velocity (units: m s^{-1}; variable name: USTAR).

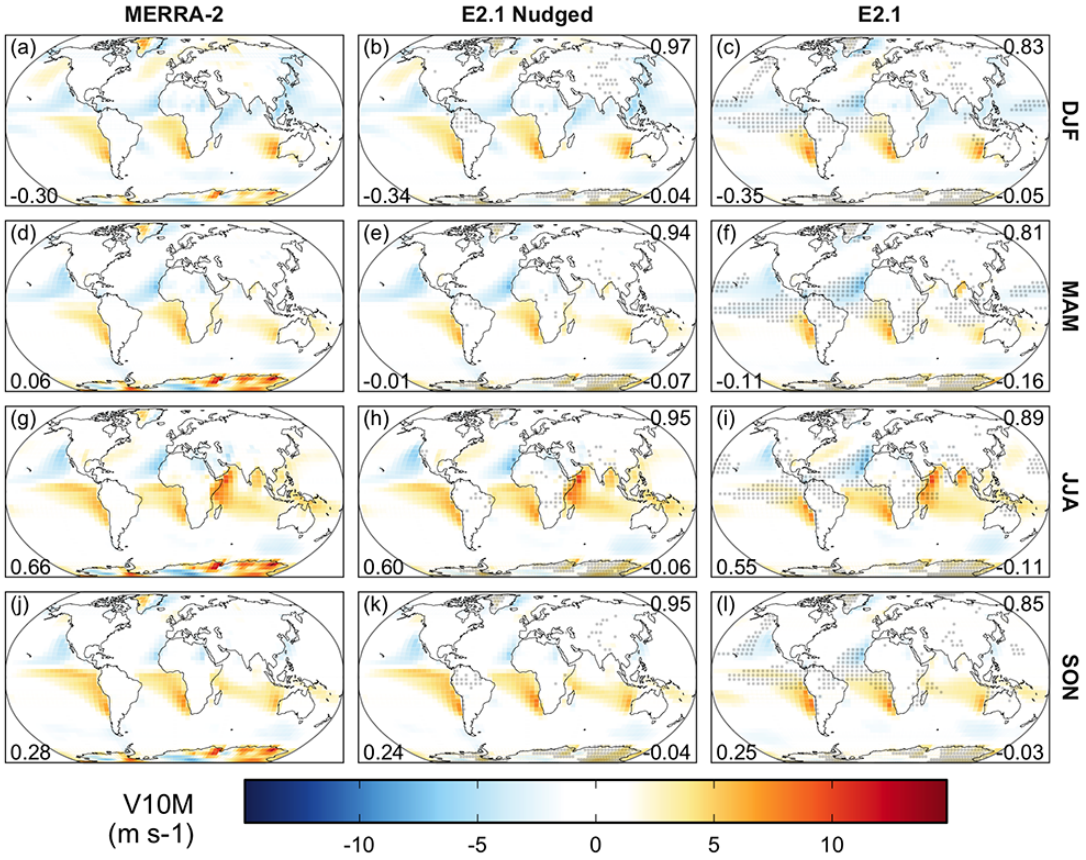

Figure S28: The same as Fig. S2, but for the meridional wind component at 10 m above the surface (units: m s^{-1}; variable name: V10M).

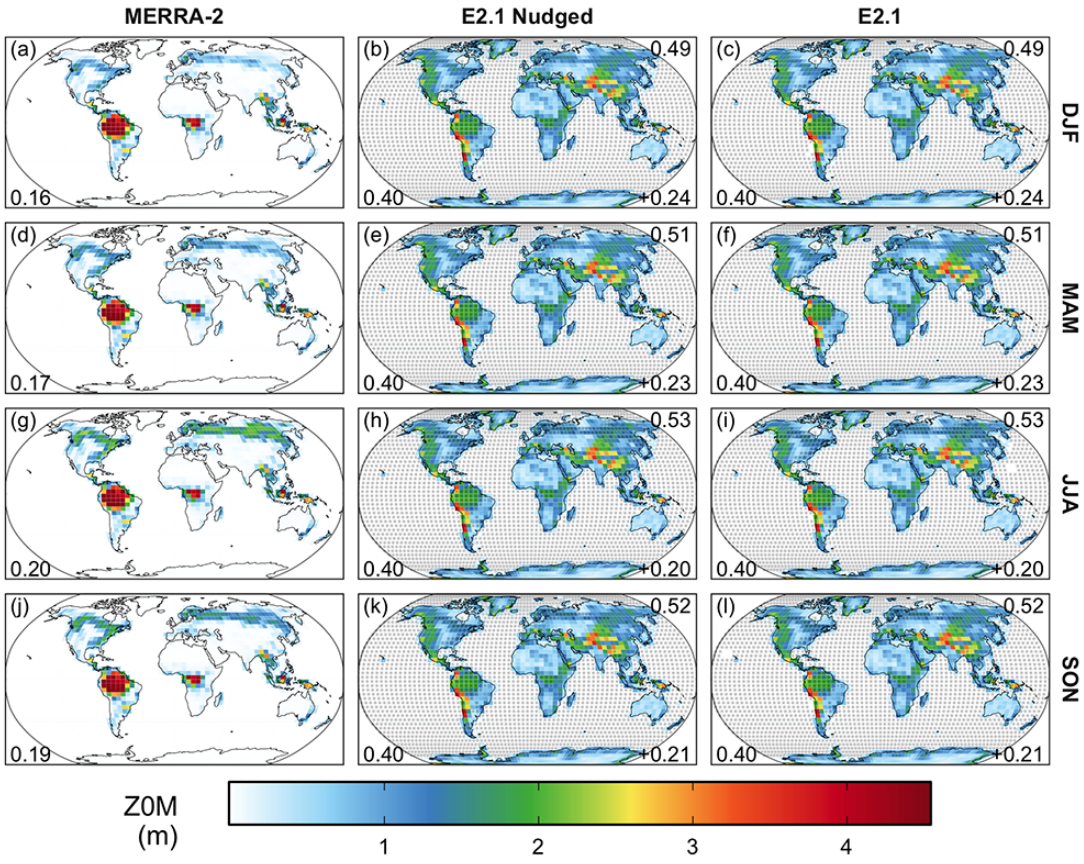

Figure S29: The same as Fig. S2, but for surface roughness (units: m; variable name: Z0M).

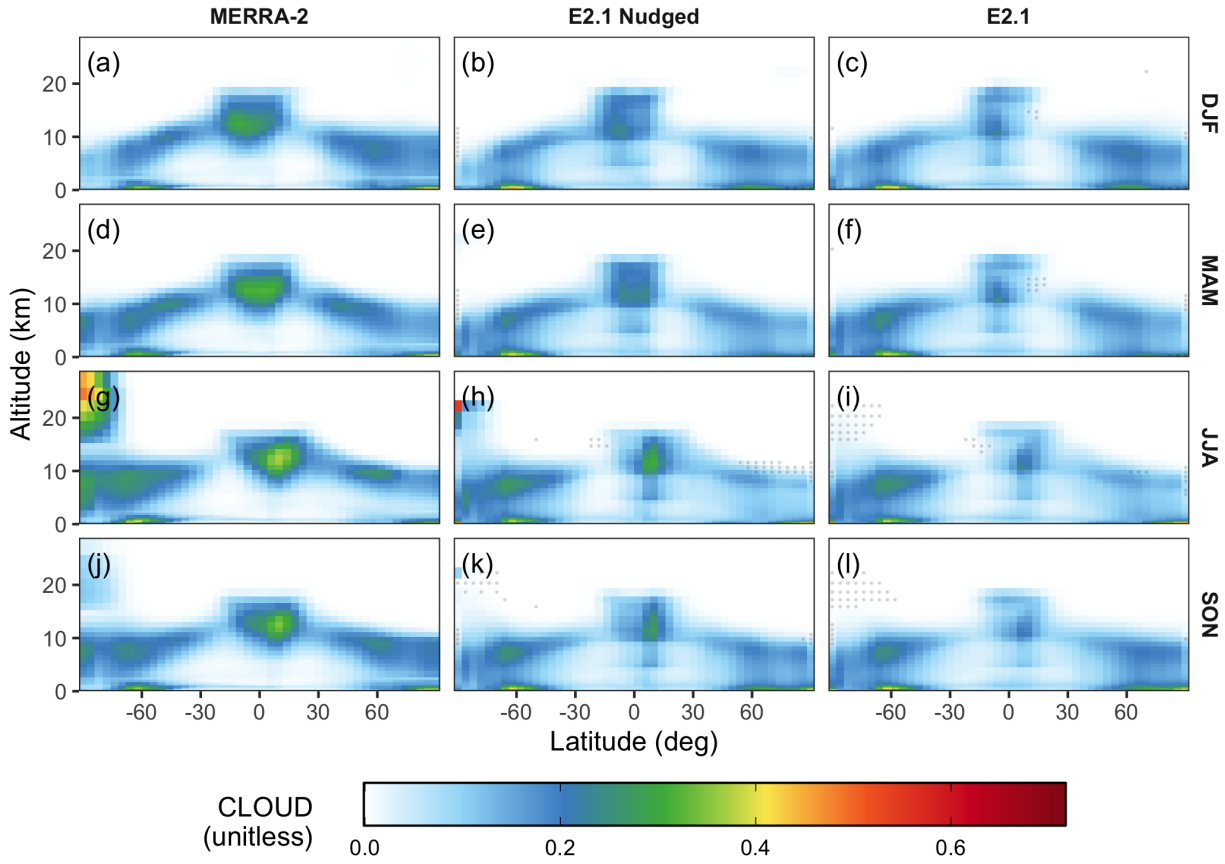

Figure S30: Seasonal zonal mean climatology of cloud fraction (unitless; variable name: CLOUD). Rows from top to bottom show the 10-year seasonal average for 2005-2014 C.E. for December-January-February (DJF), March-April-May (MAM), June-July-August (JJA), and September-October-November (SON). Columns from left to right show the values from the MERRA-2 reanalysis (Gelaro et al., 2017), E2.1 nudged to MERRA-2, and the free-running E2.1. Gray dots indicate locations where the E2.1 simulations are statistically different with respect to interannual variability (p-value < 0.05; $n = 10$ yr).

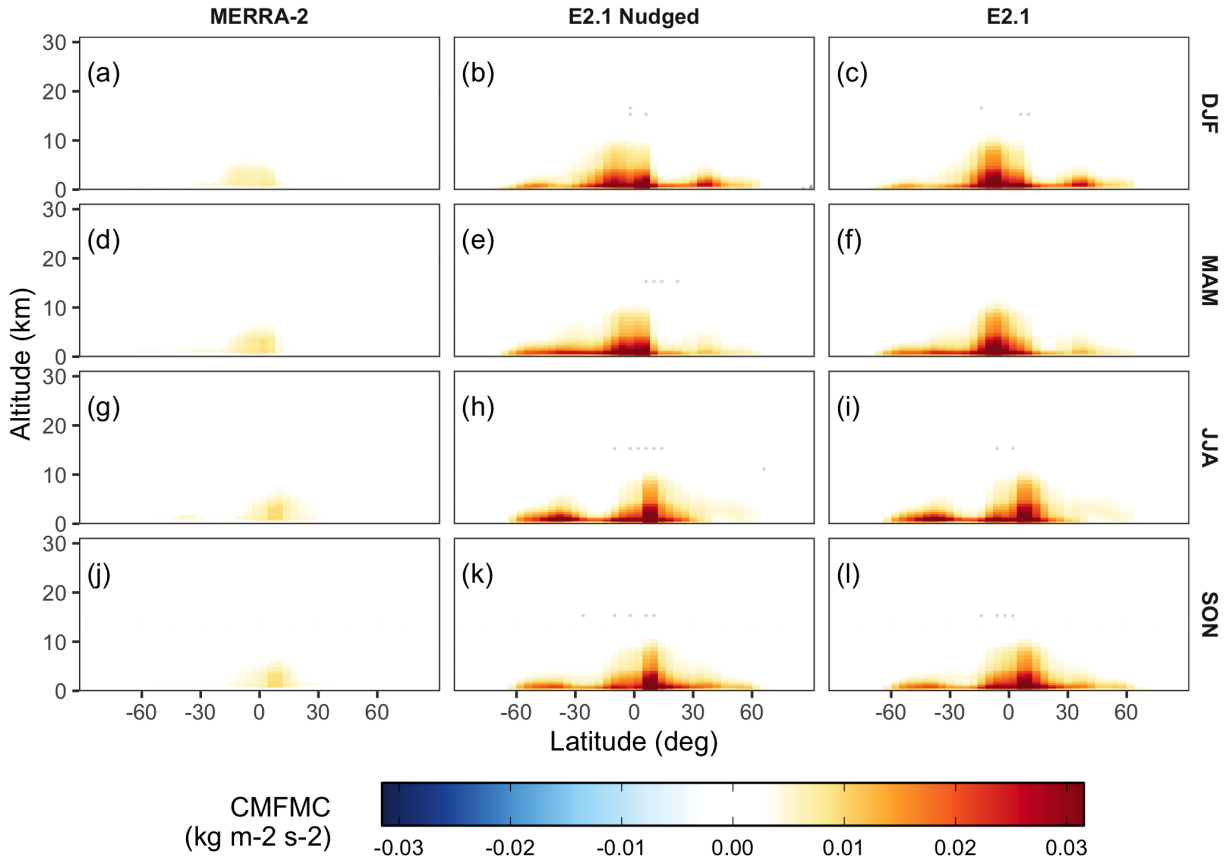

Figure S31: The same as Fig. S30, but for the zonal mean upward moist convective mass flux (units: kg $m^{-2\ -1}$; variable name: CMFMC).

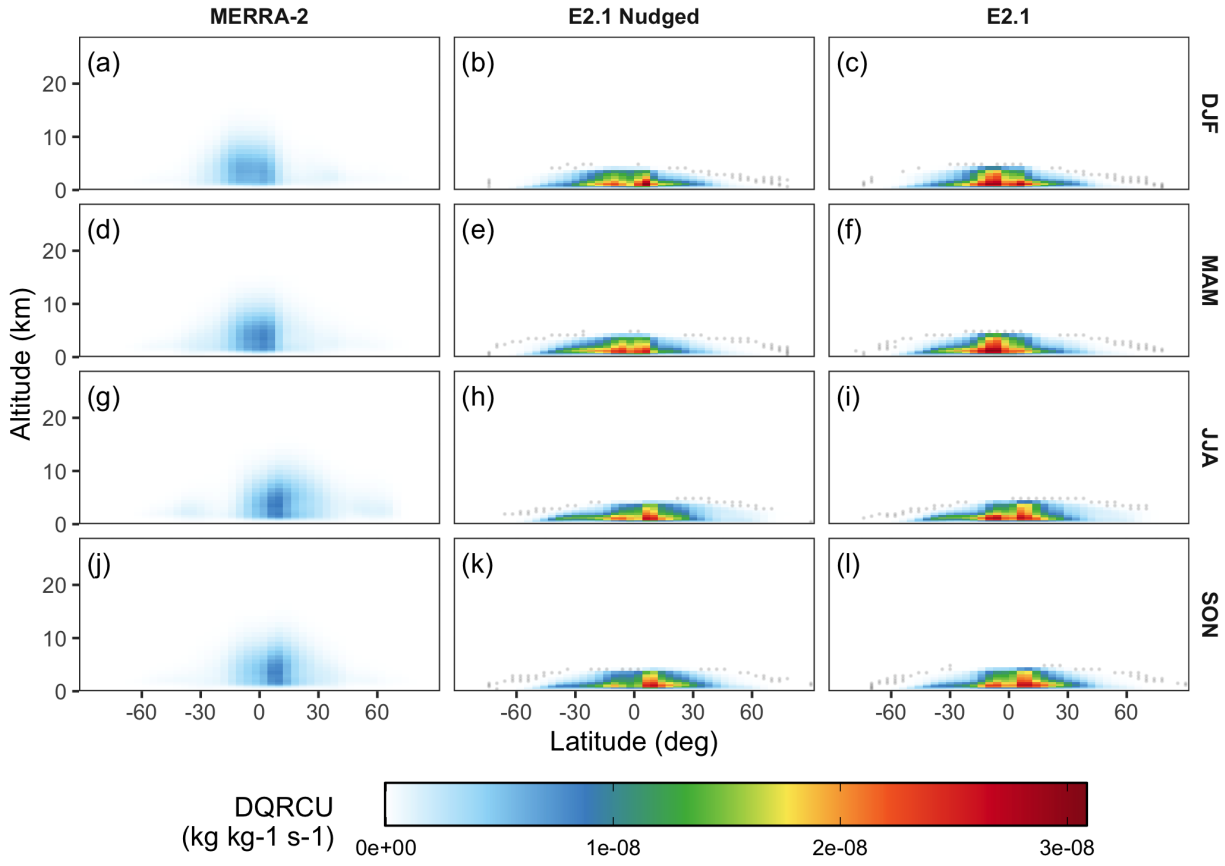

Figure S32: The same as Fig. S30, but for the zonal mean convective precipitation source (units: kg kg^{-1} s^{-1}; variable name: DQRCU).

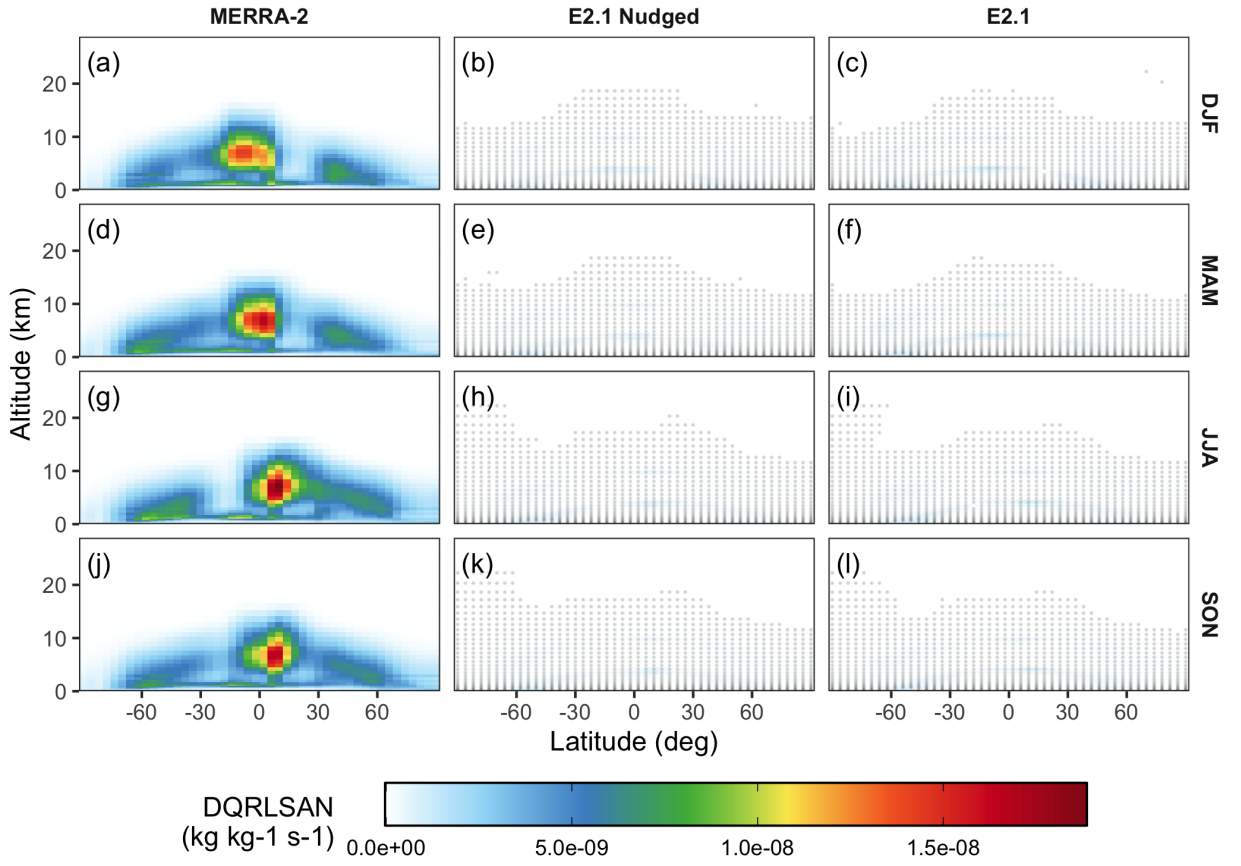

Figure S33: The same as Fig. S30, but for the zonal mean stratiform and anvil precipitation source (units: kg kg^{-1} s^{-1}; variable name: DQRLSAN).

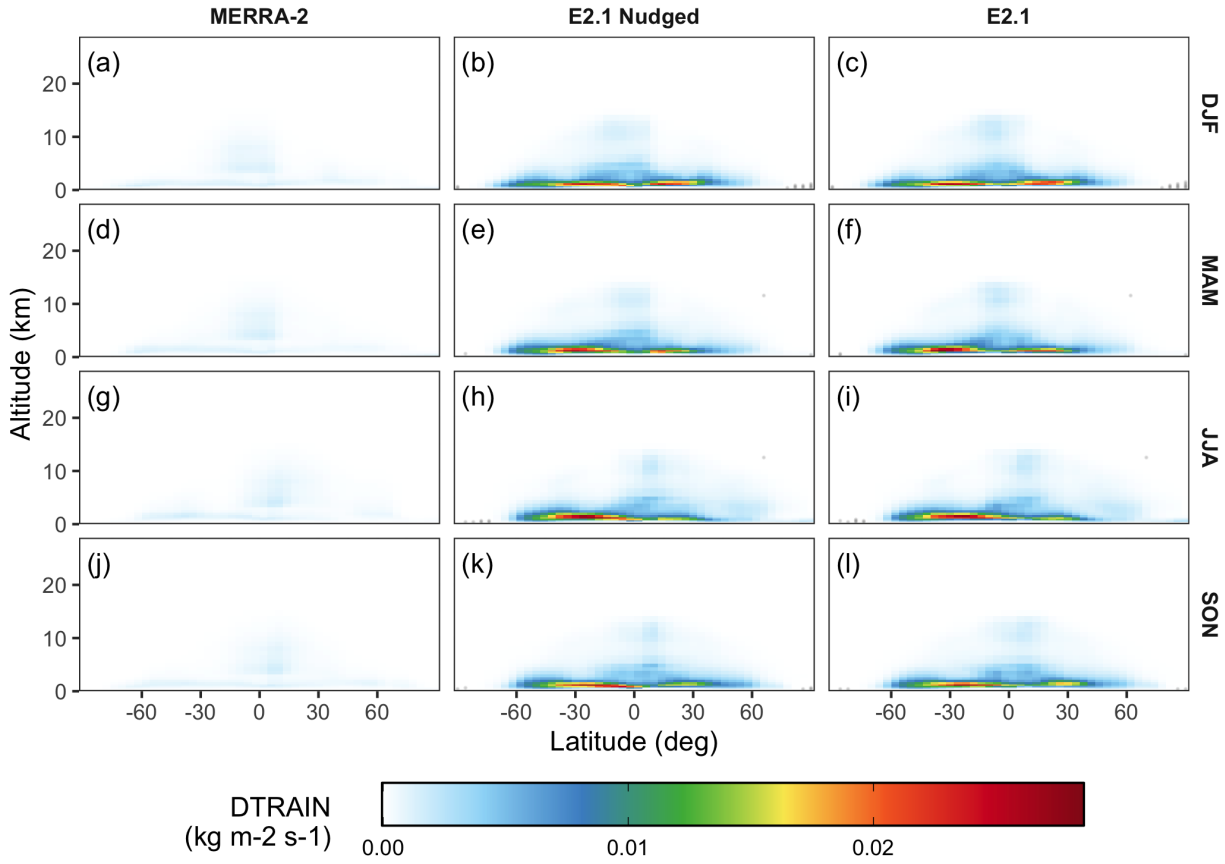

Figure S34: The same as Fig. S30, but for the zonal mean detraining mass flux (units: kg m^{-2} s^{-1}; variable name: DTRAIN).

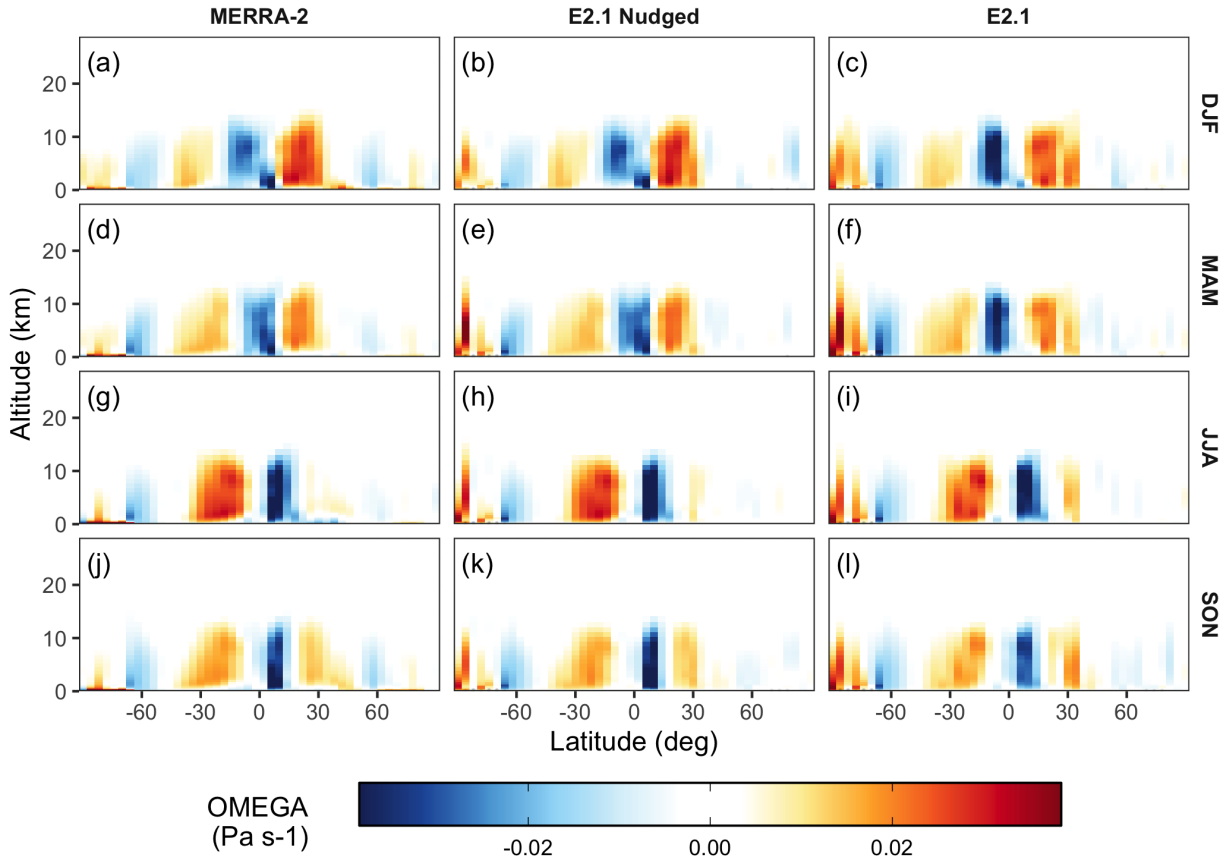

Figure S35: The same as Fig. S30, but for the zonal mean vertical pressure velocity (units: Pa s^{-1}; variable name: OMEGA).

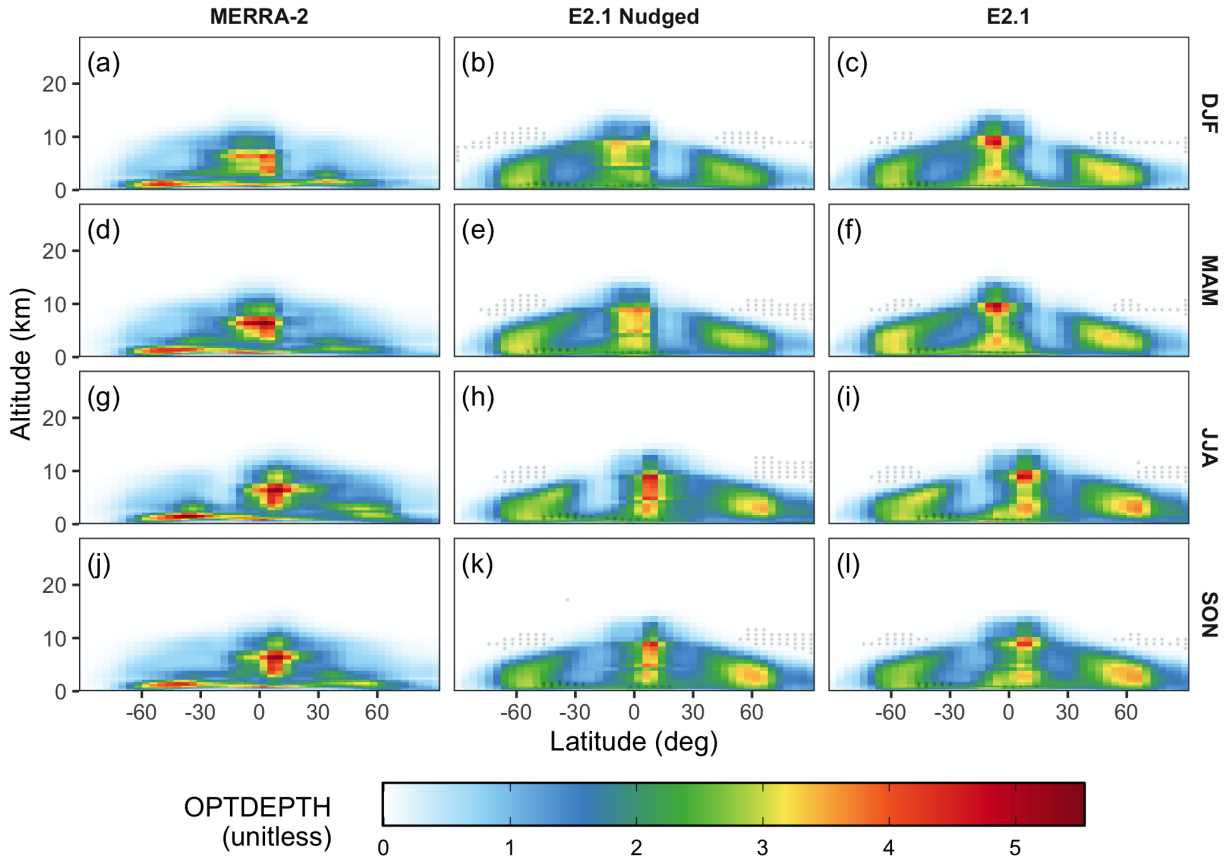

Figure S36: The same as Fig. S30, but for the zonal mean in-cloud optical depth (unitless; variable name: OPTDEPTH).

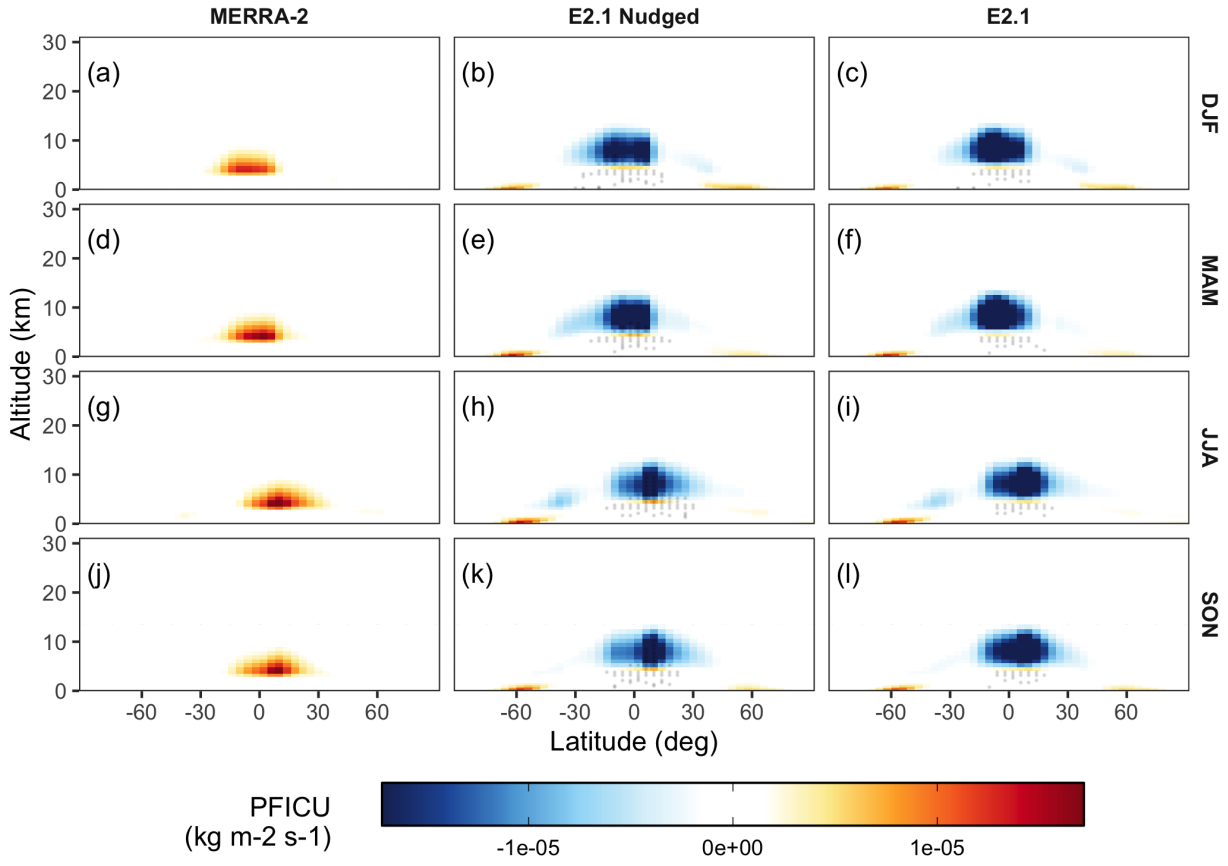

Figure S37: The same as Fig. S30, but for the zonal mean flux of ice precipitation from convection (units: kg $m^{-2\ -1}$; variable name: PFICU).

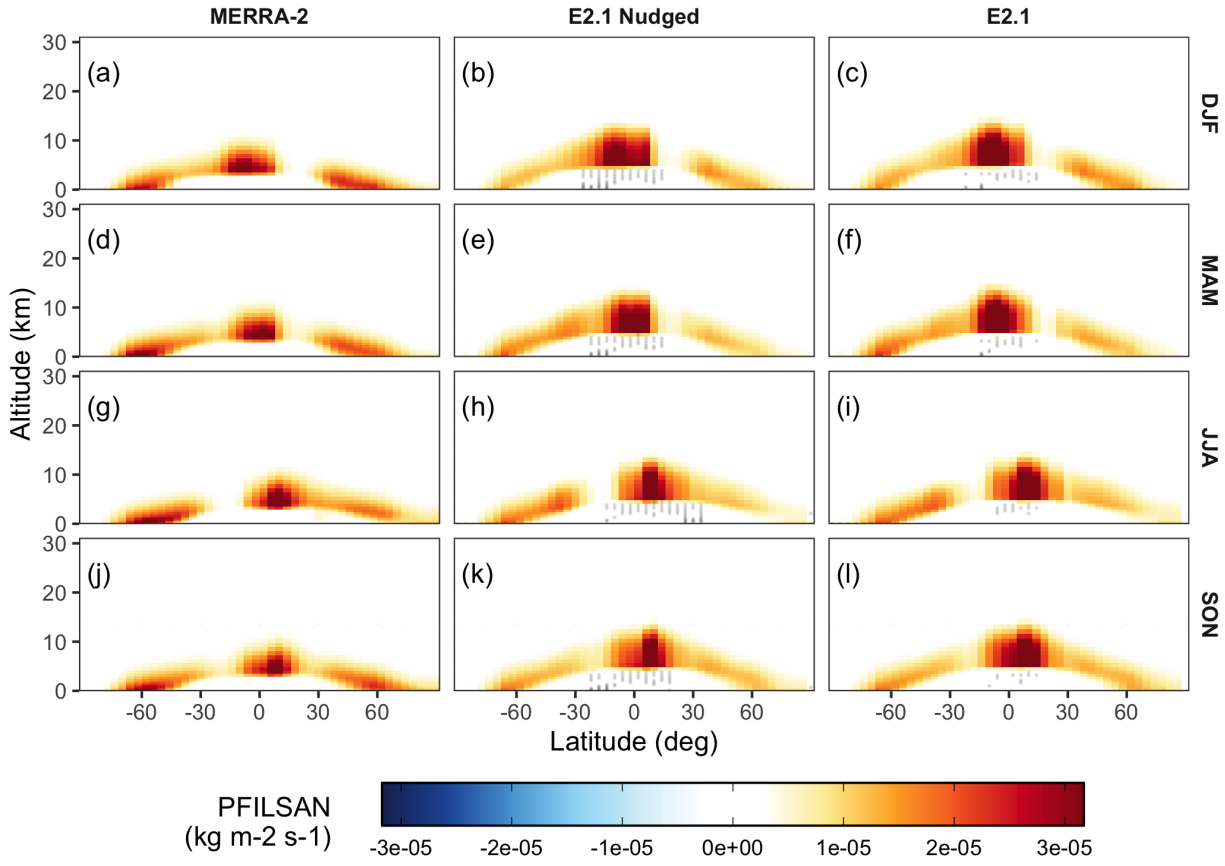

Figure S38: The same as Fig. S30, but for the zonal mean flux of ice precipitation from stratiform clouds (units: kg m^{-2} $^{-1}$; variable name: PFILSAN).

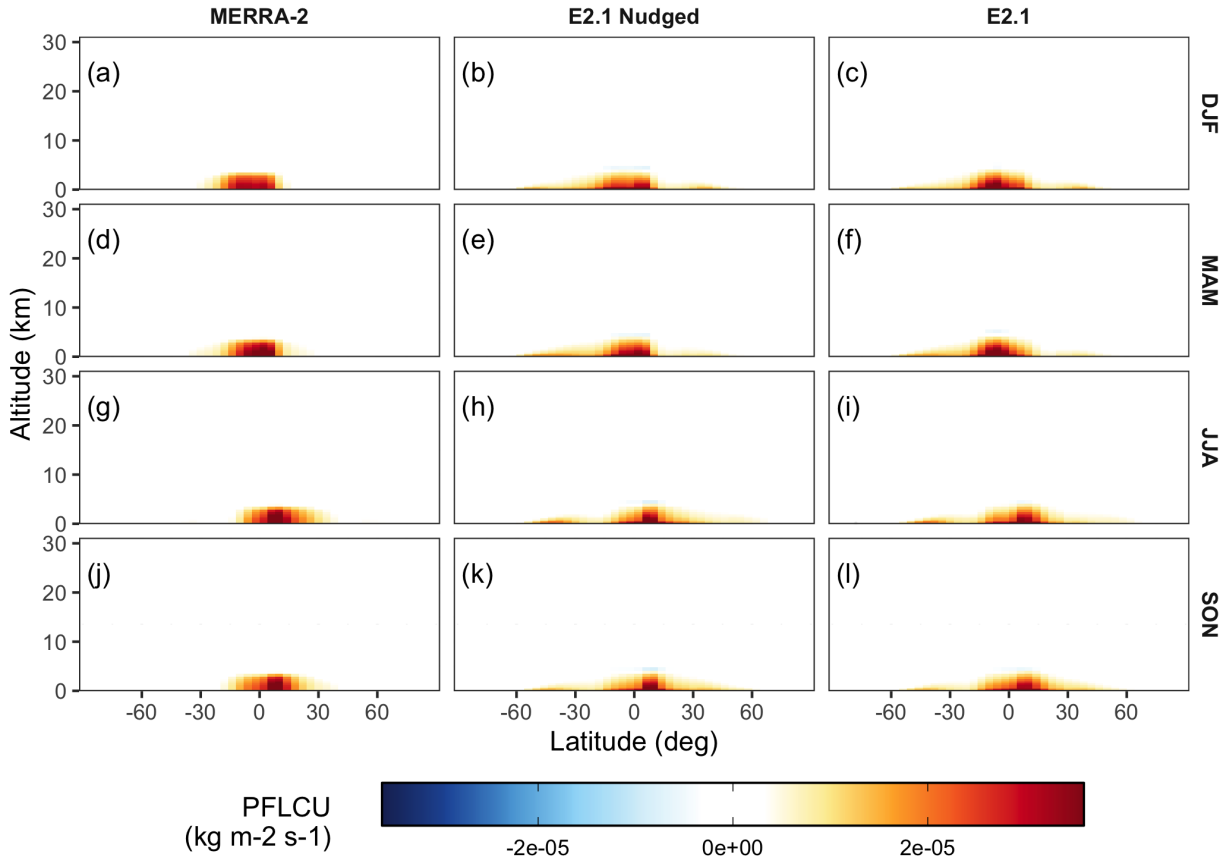

Figure S39: The same as Fig. S30, but for the zonal mean flux of liquid precipitation from convection (units: kg $m^{-2\ -1}$; variable name: PFLCU).

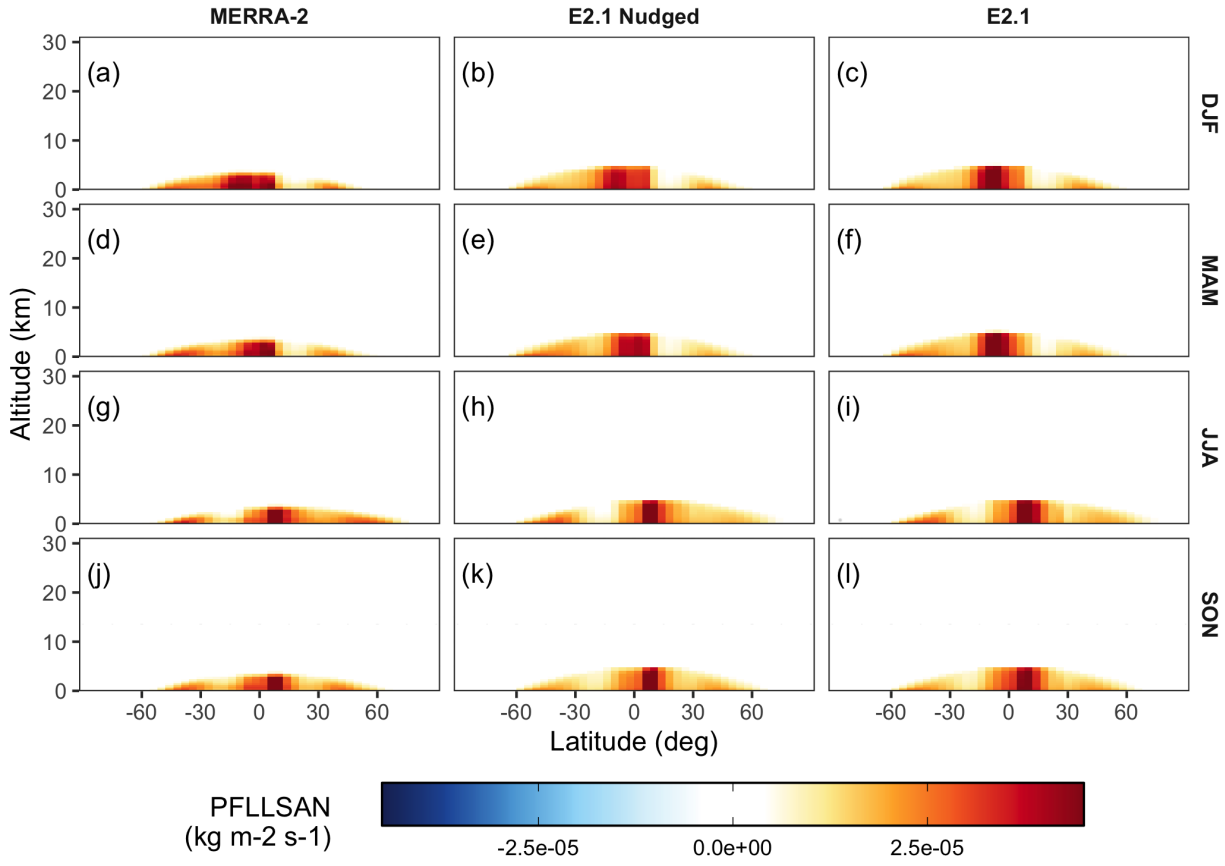

Figure S40: The same as Fig. S30, but for the zonal mean flux of liquid precipitation from stratiform clouds (units: kg m^{-2} $^{-1}$; variable name: PFLLSAN).

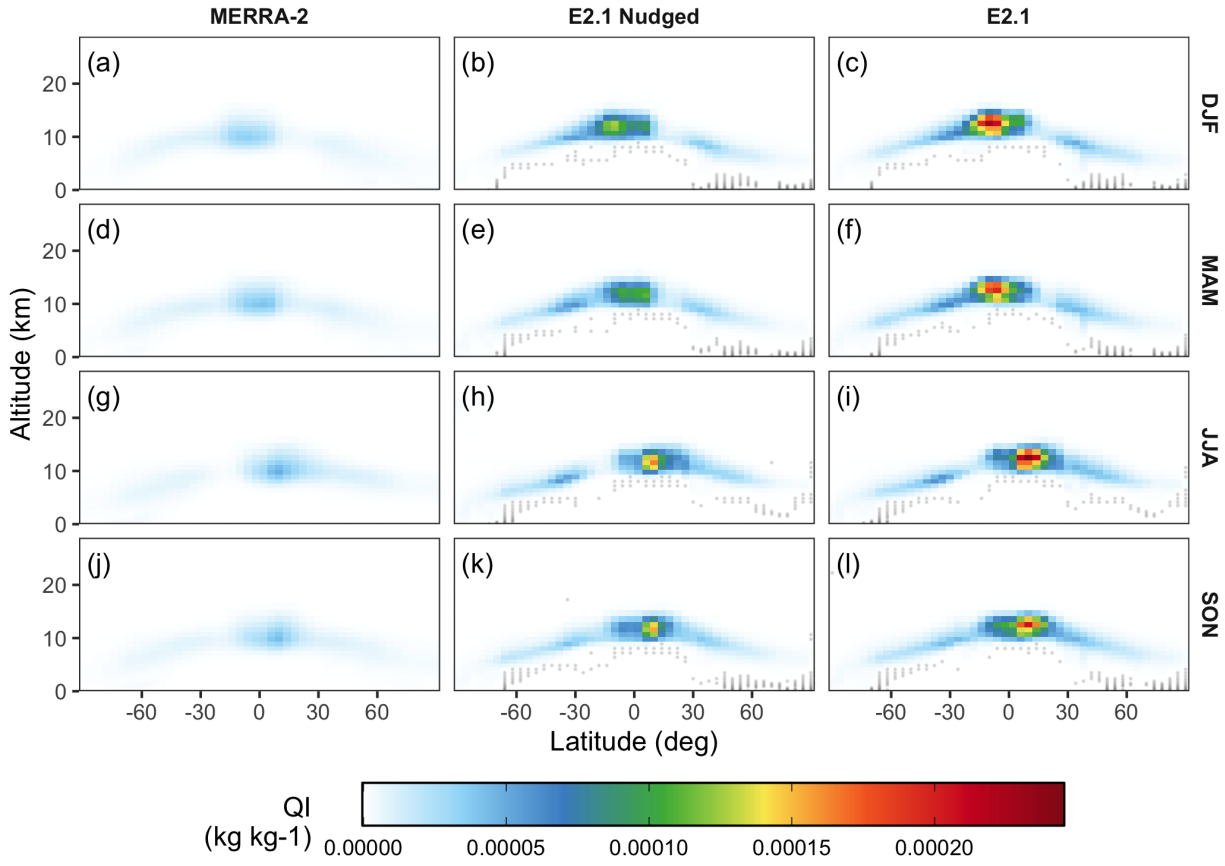

Figure S41: The same as Fig. S30, but for the zonal mean mass fraction of cloud ice water (units: kg kg^{-1}; variable name: QI).

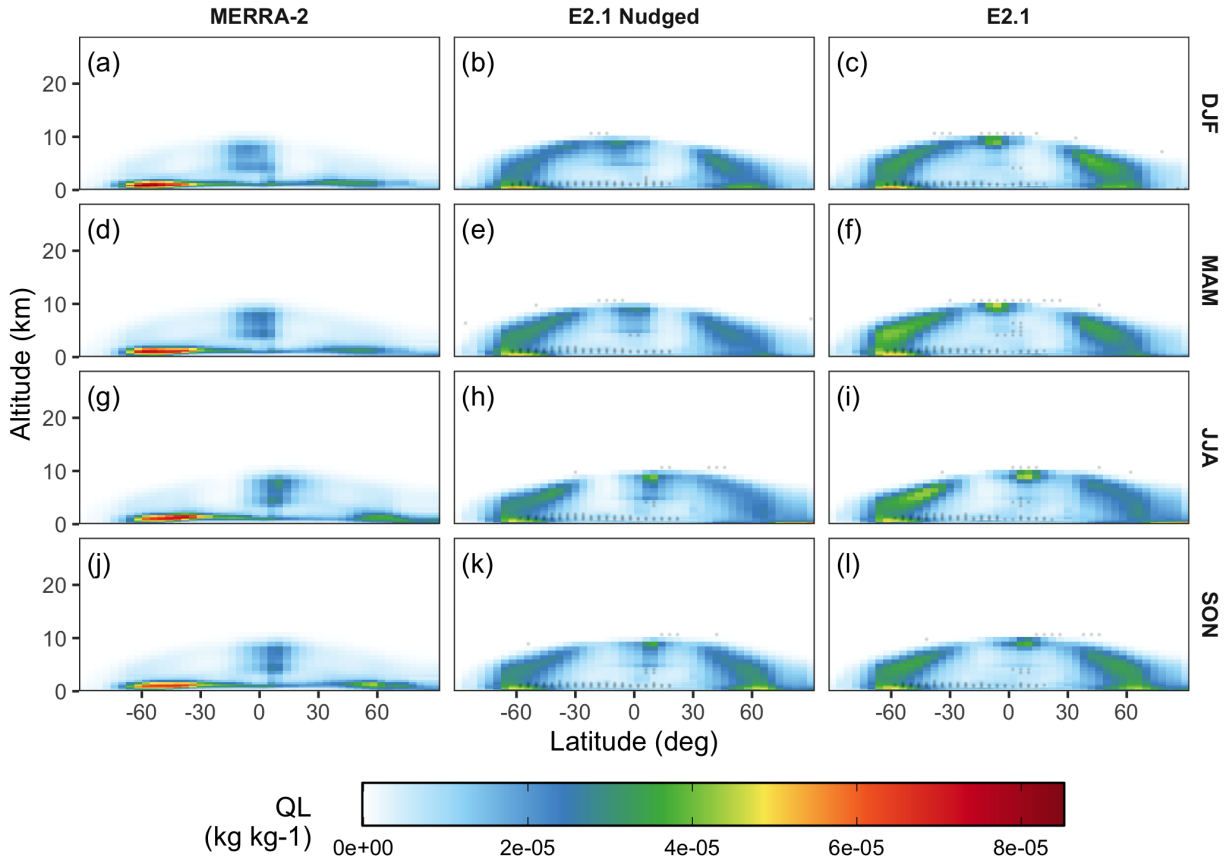

Figure S42: The same as Fig. S30, but for the zonal mean mass fraction of cloud liquid water (units: kg kg^{-1}; variable name: QL).

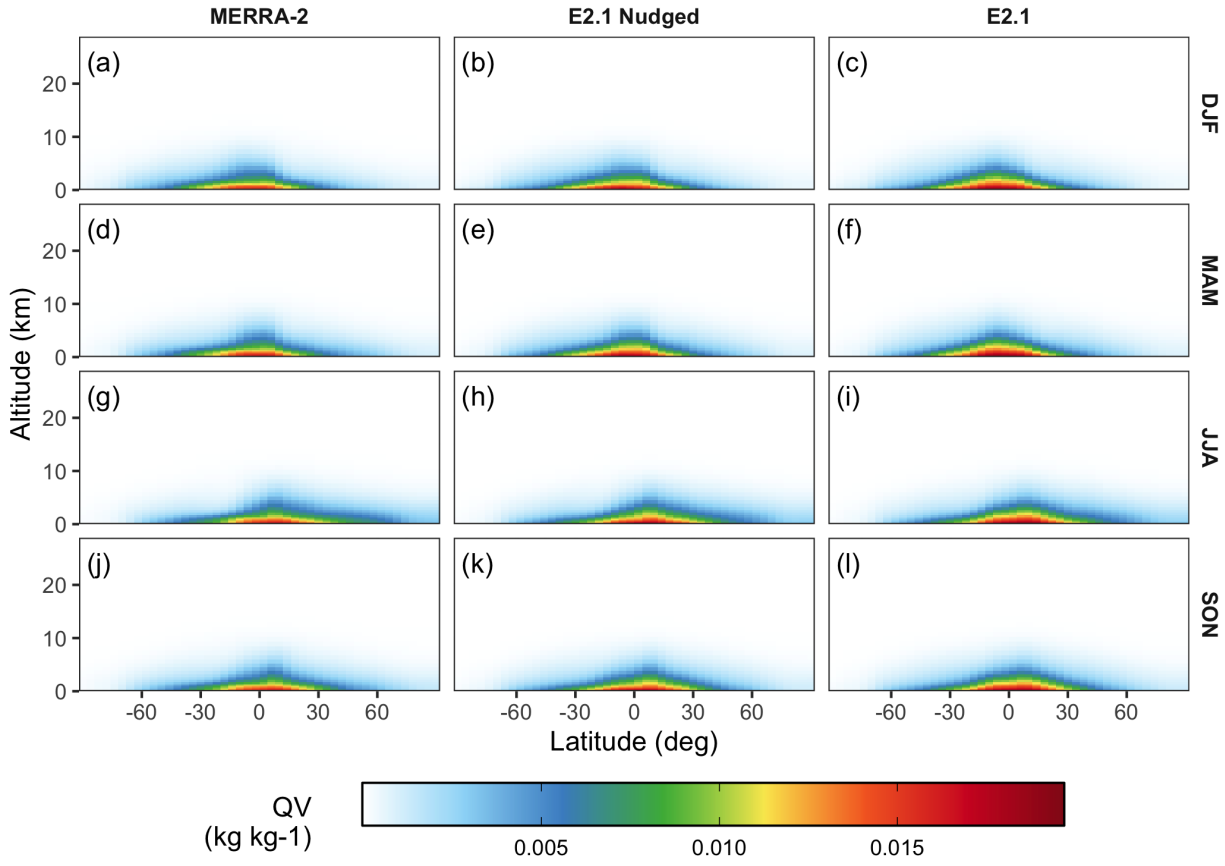

Figure S43: The same as Fig. S30, but for the zonal mean specific humidity (units: kg kg^{-1}; variable name: QV).

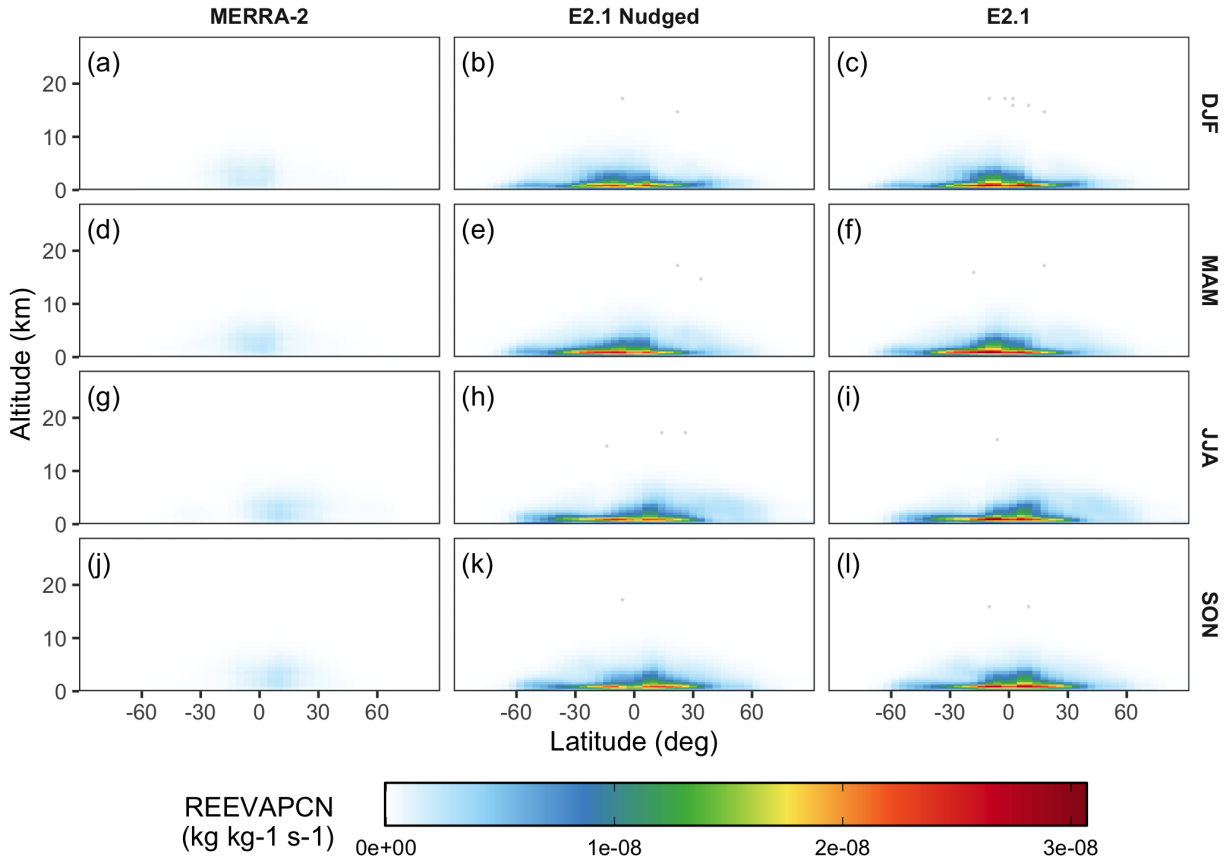

Figure S44: The same as Fig. S30, but for the zonal mean evaporation and sublimation of convective precipitation (units: kg kg^{-1} s^{-1}; variable name: REEVAPCN).

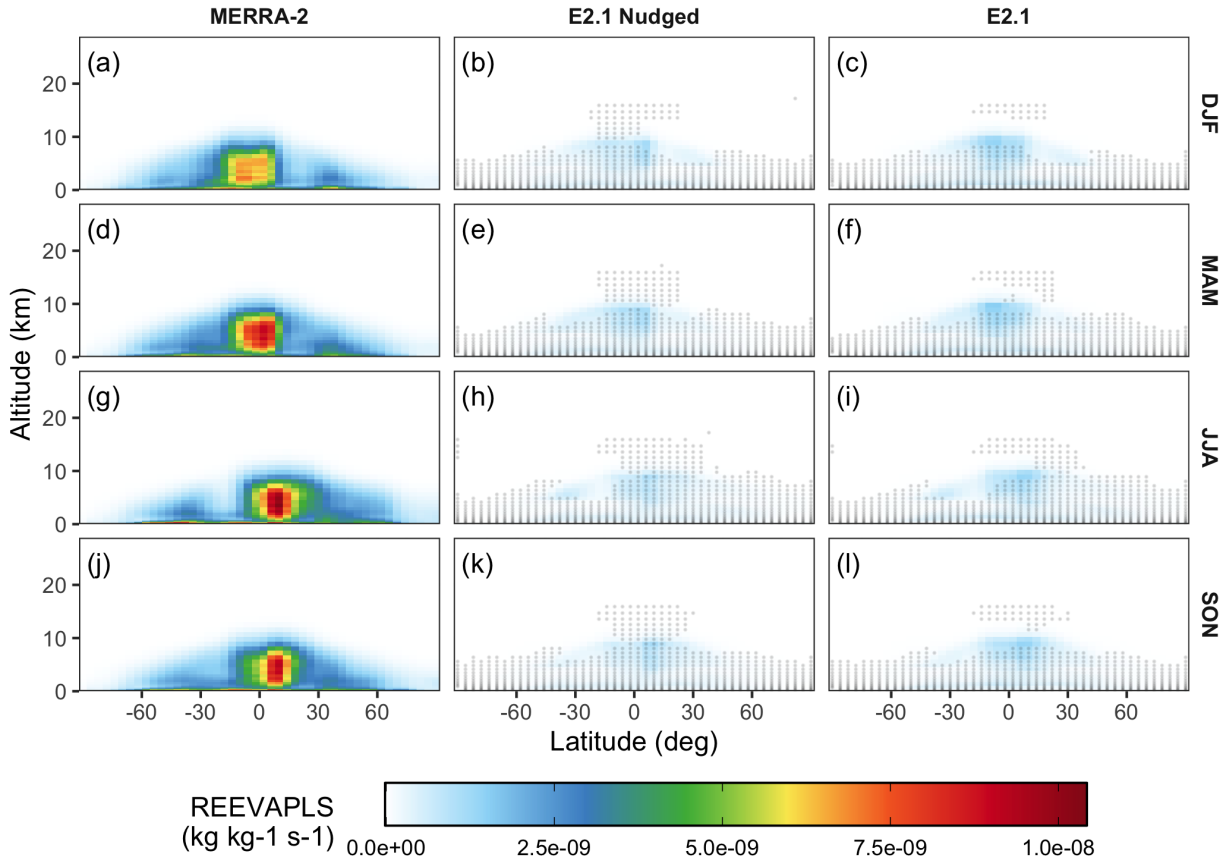

Figure S45: The same as Fig. S30, but for the zonal mean evaporation and sublimation of stratiform and anvil precipitation (units: kg kg^{-1} s^{-1}; variable name: REEVAPLS).

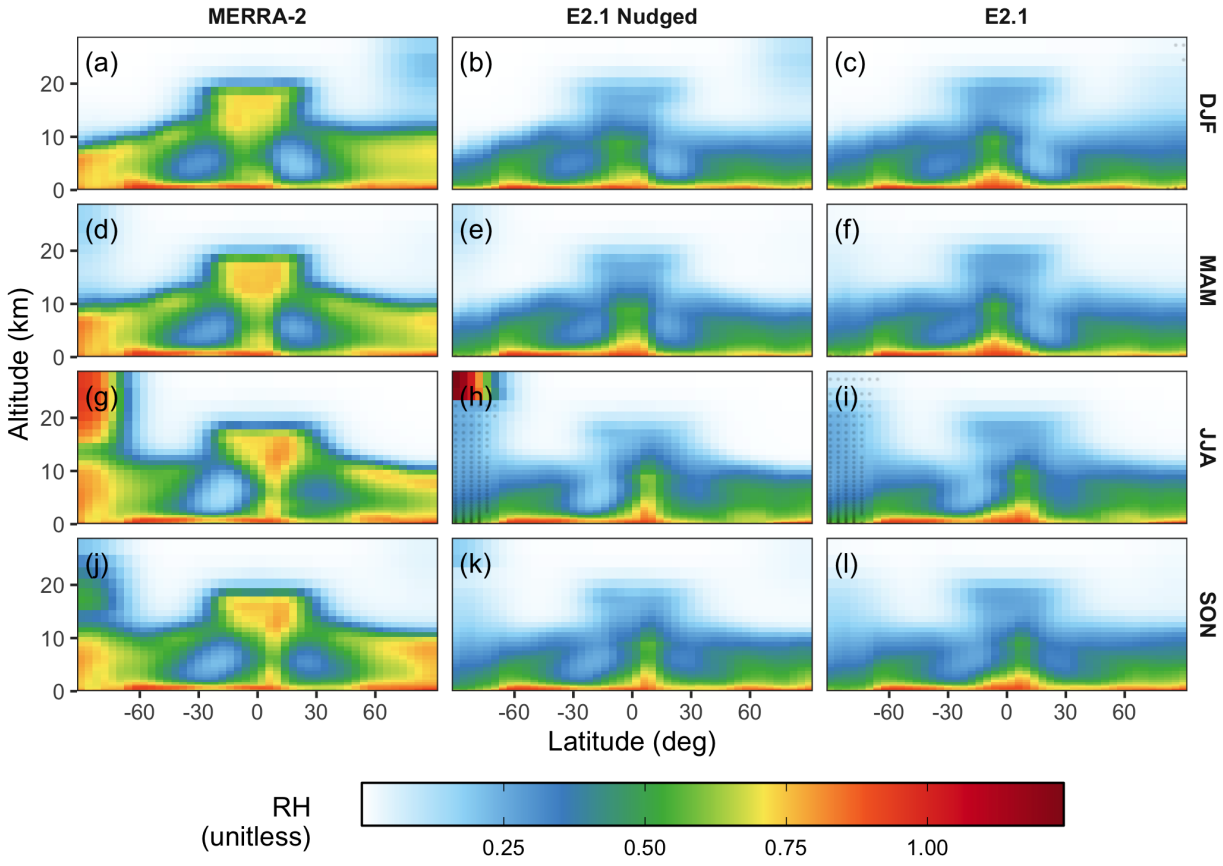

Figure S46: The same as Fig. S30, but for the zonal mean relative humidity (unitless; variable name: RH).

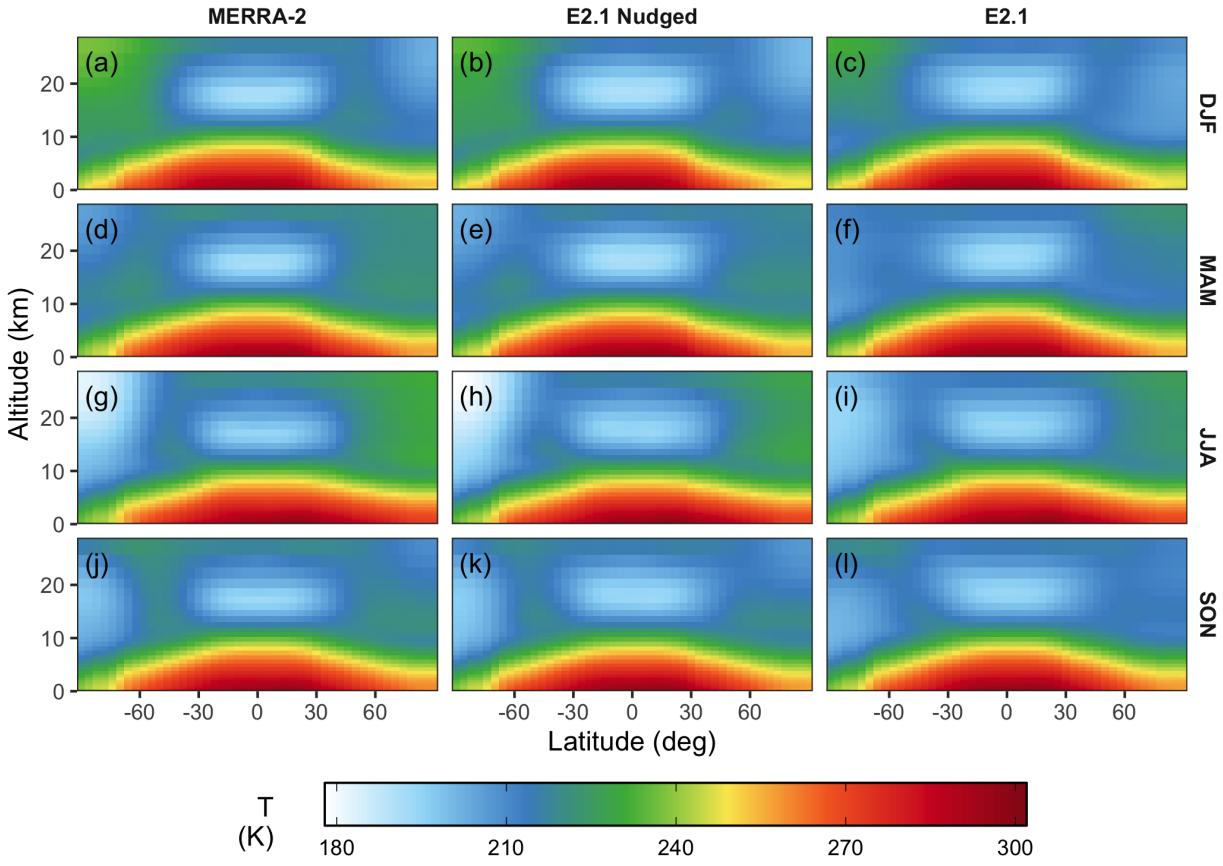

Figure S47: The same as Fig. S30, but for the zonal mean temperature (units: K; variable name: T).

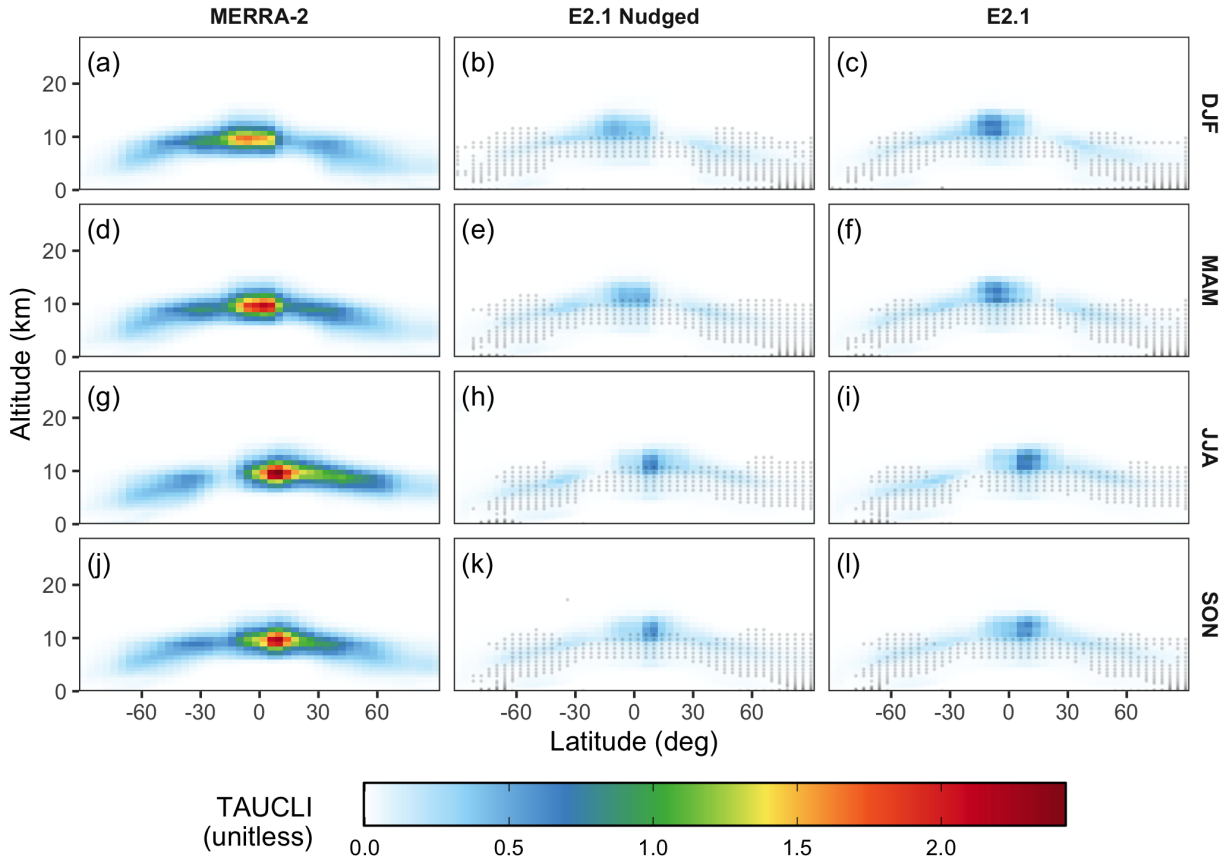

Figure S48: The same as Fig. S30, but for the zonal mean in-cloud optical thickness of ice clouds (unitless; variable name: TAUCLI).

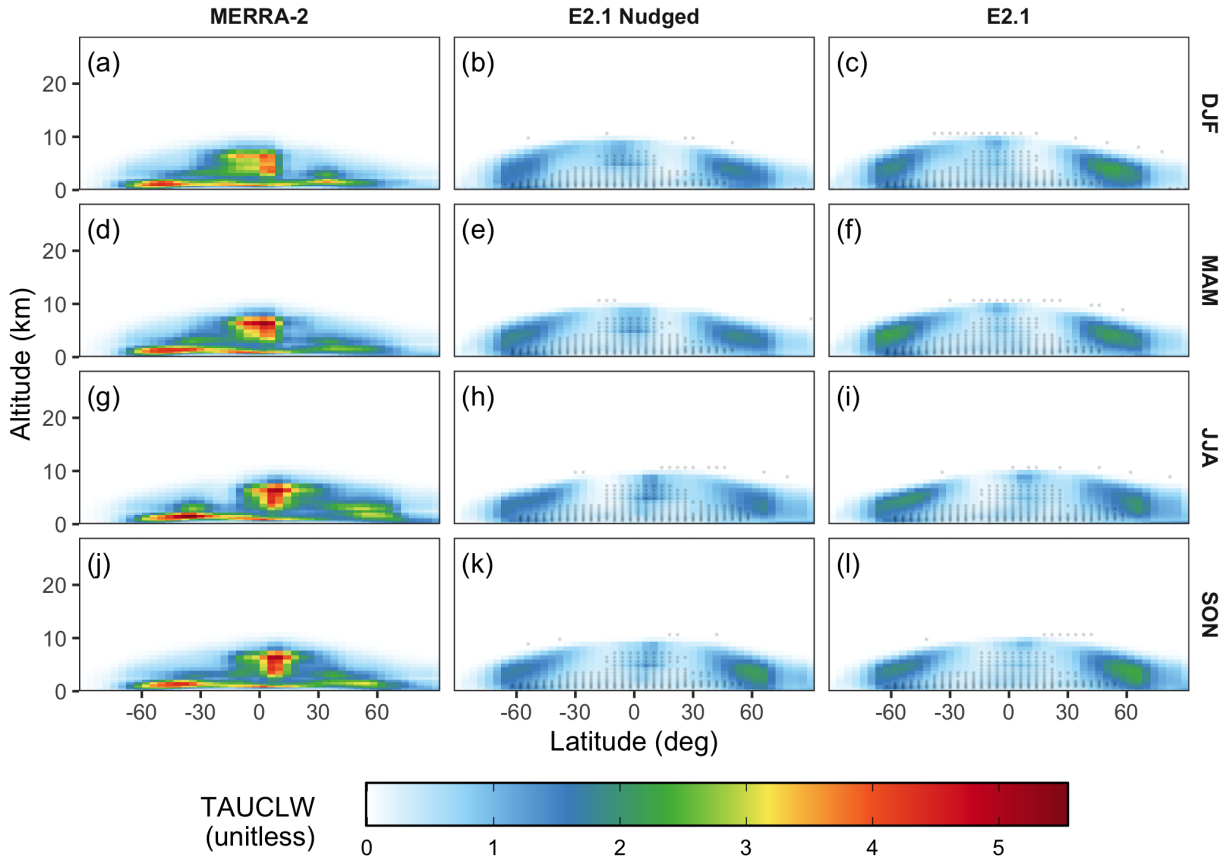

Figure S49: The same as Fig. S30, but for the zonal mean in-cloud optical thickness of liquid clouds (unitless; variable name: TAUCLW).

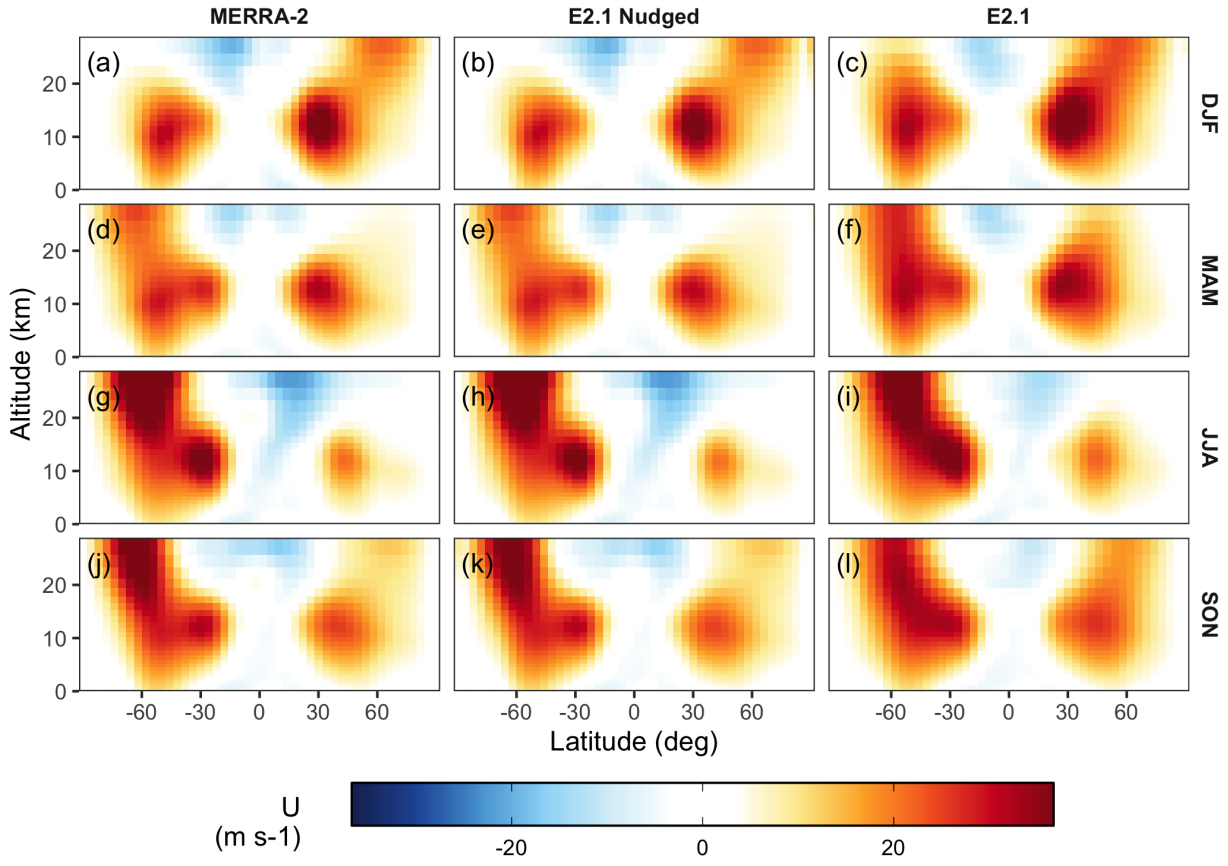

Figure S50: The same as Fig. S30, but for the zonal mean zonal wind component (units: m s^{-1}; variable name: U).

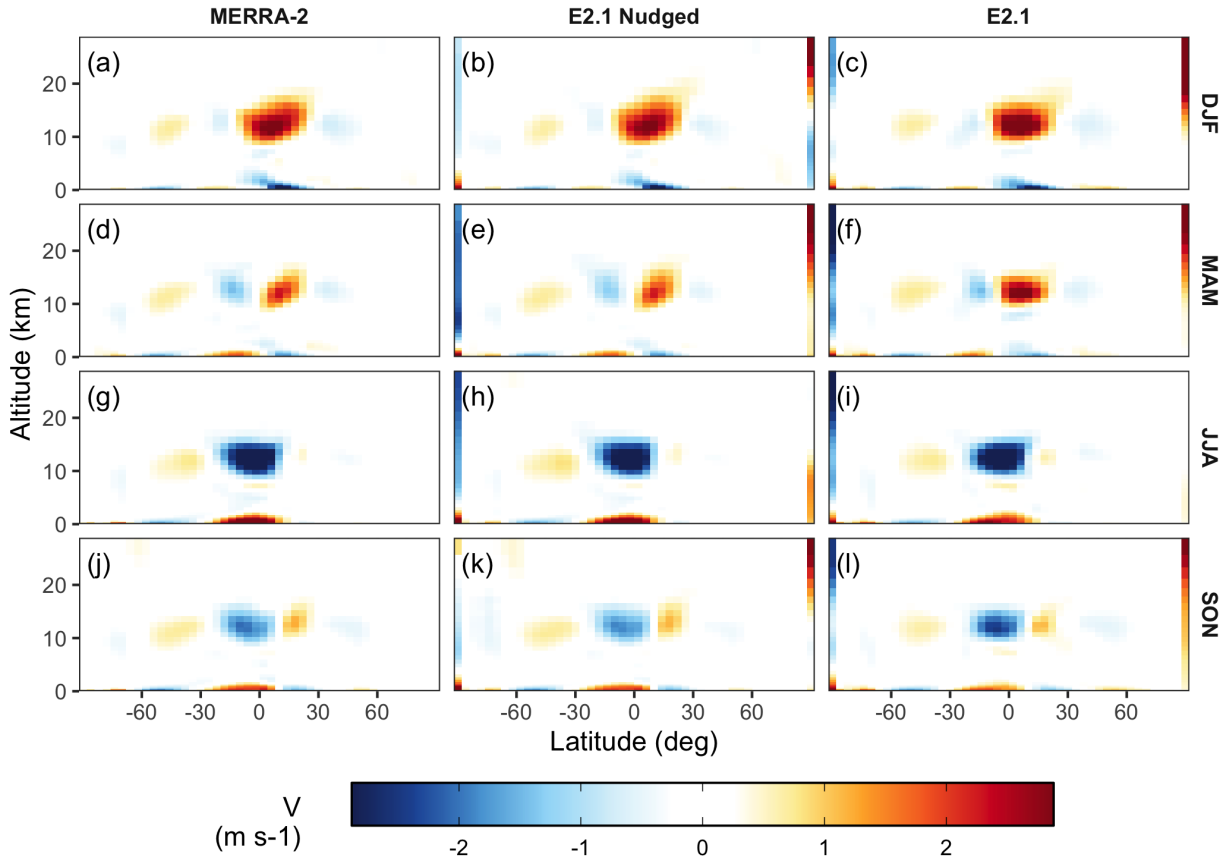

Figure S51: The same as Fig. S30, but for the zonal mean meridional wind component (units: m s^{-1}; variable name: V).

S2 Emissions

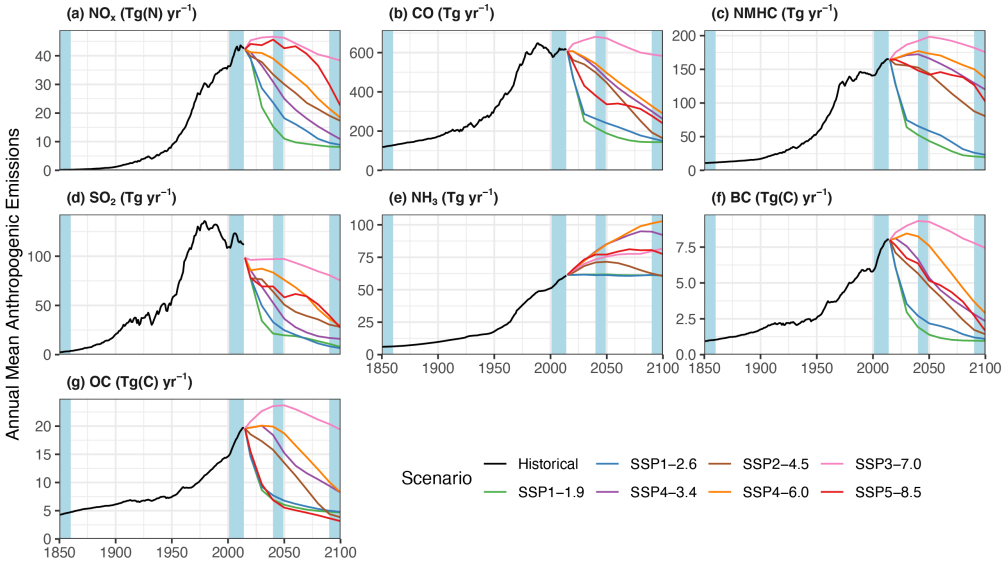

Figure S52: The same as Fig. 6 in the main text, but isolating surface anthropogenic emissions excluding open fires.

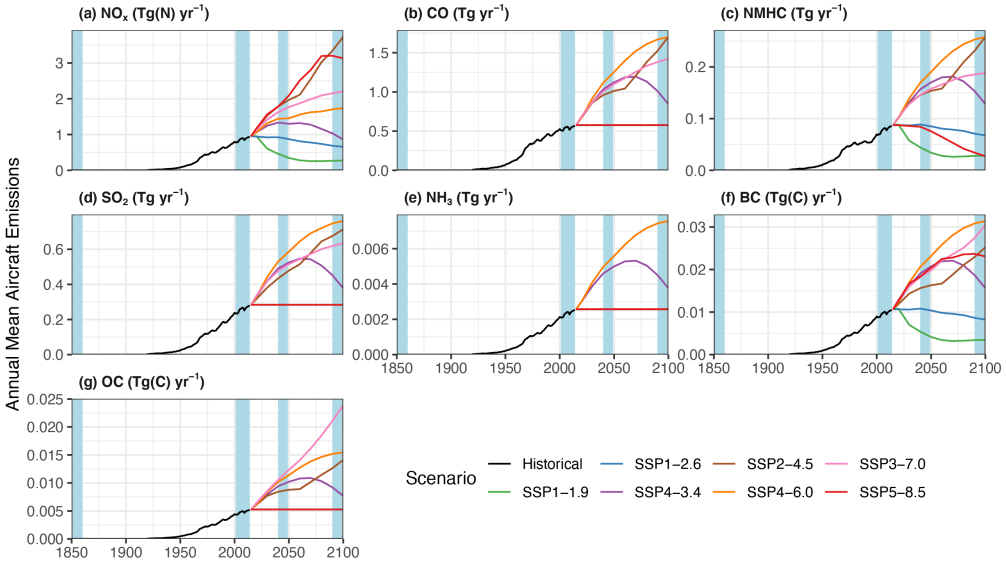

Figure S53: The same as Fig. S52, but isolating aircraft emissions.

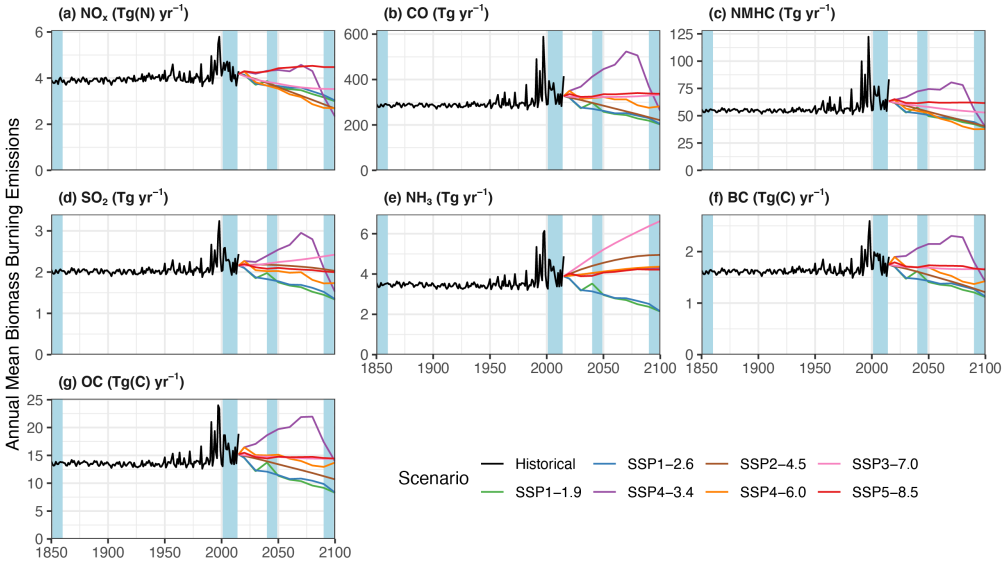

Figure S54: The same as Fig. S52, but isolating open fire emissions. Historical emissions are from van Marle et al. (2017) and future emissions from Gidden et al. (2019).

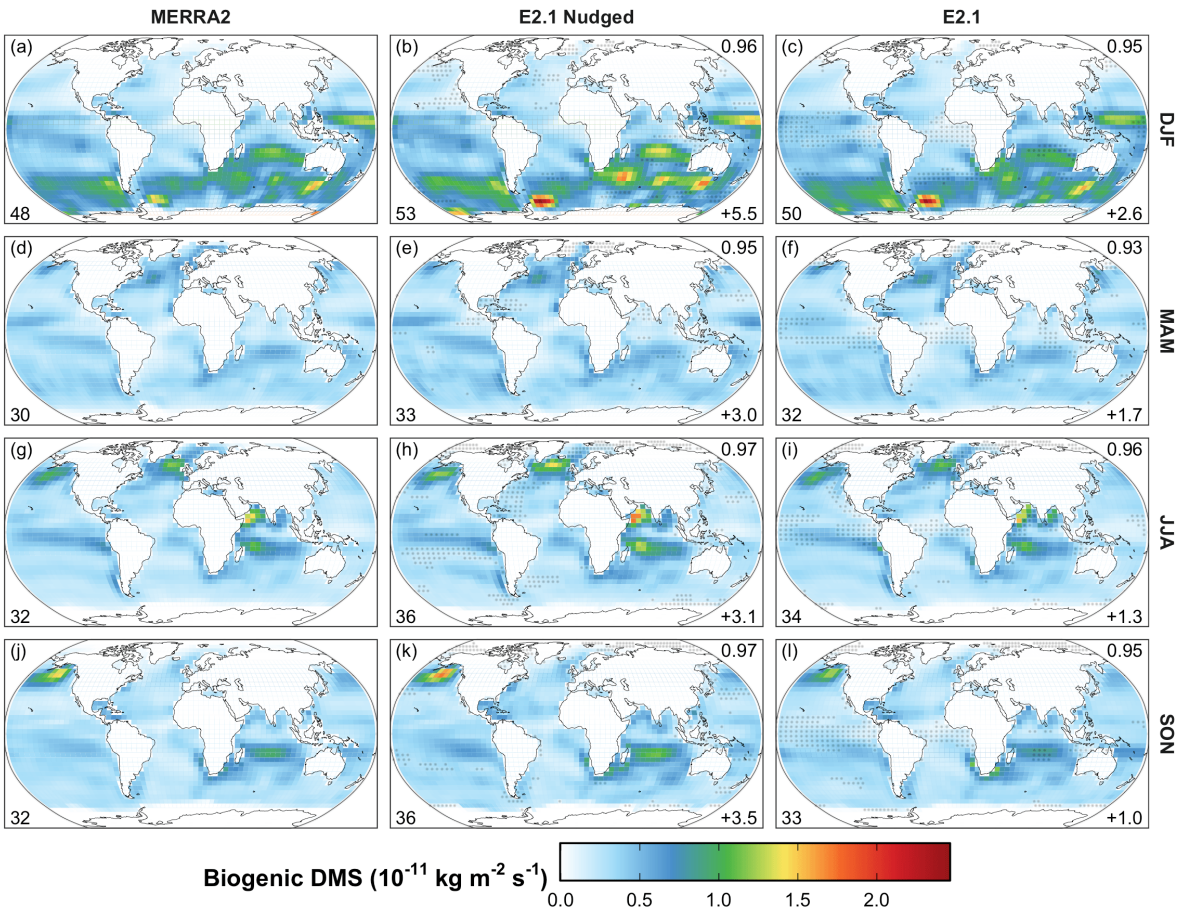

Figure S55: Seasonal mean spatial distribution of dimethylsulfide ($(CH_3)_2S$; DMS) emissions from marine biogenic activity for 2005-2014 C.E. Each column from left to right shows emission fluxes calculated using: MERRA-2 meteorology, E2.1 meteorology nudged to MERRA-2, and the free-running E2.1 meteorology, respectively. Each row from top to bottom shows mean emission fluxes for December-January-February (DJF), March-April-May (MAM), June-July-August (JJA), and September-October-November (SON). Gray dots indicate locations where the E2.1-driven simulations show statistically significant differences (p-value < 0.05; $n = 10$ seasons) with respect to the MERRA-2-driven simulation. The value in the lower left of each panel gives the globally integrated source in Tg a^{-1}. The number in the lower (upper) right of each panel gives the total difference (pattern correlation) of the E2.1-driven simulations with respect to their respective MERRA-2-driven values.

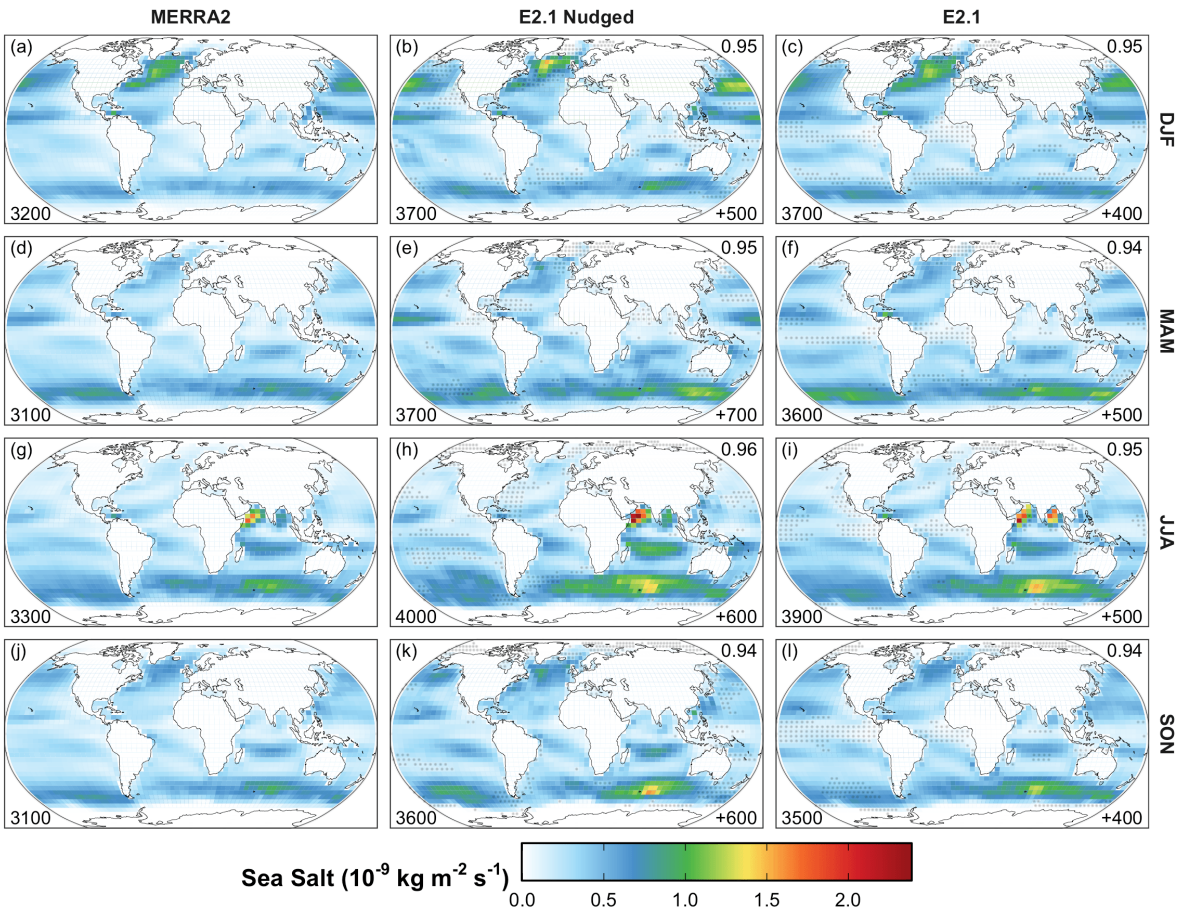

Figure S56: Same as **Fig. S55**, but for aeolian sea salt emissions.

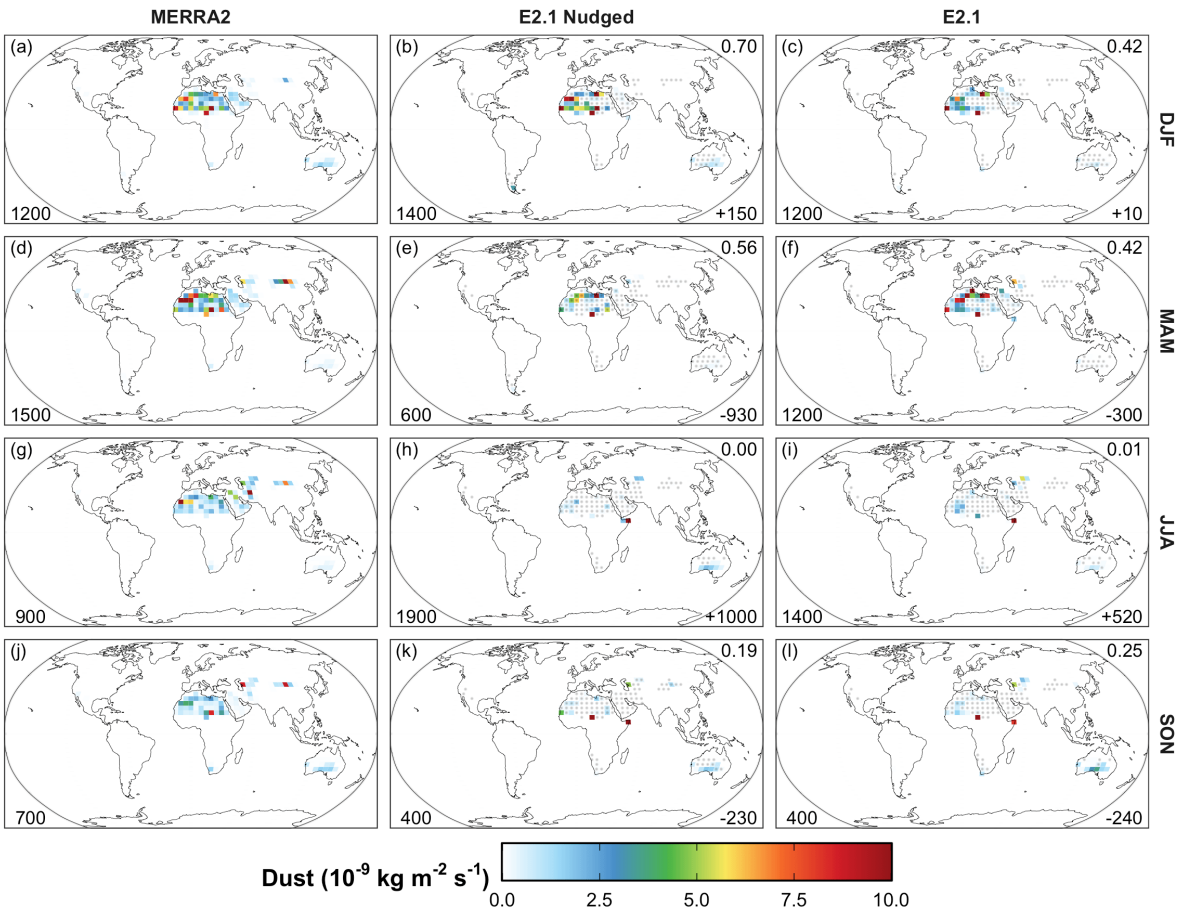

Figure S57: Same as **Fig. S55**, but for aeolian mineral dust emissions.

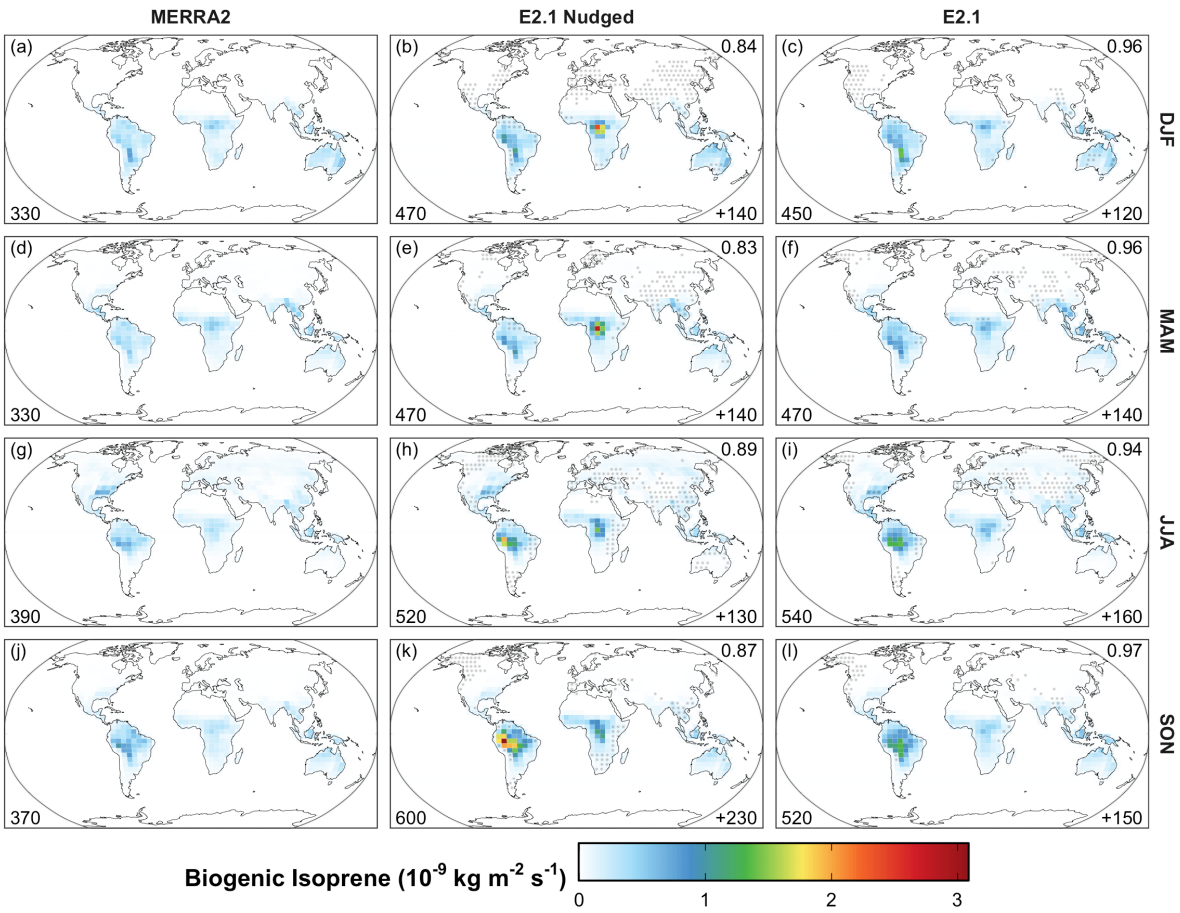

Figure S58: Same as **Fig. S55**, but for isoprene (2-methyl-1,3-butadiene; $CH_2=C(CH_3)CH=CH_2$) from terrestrial plants.

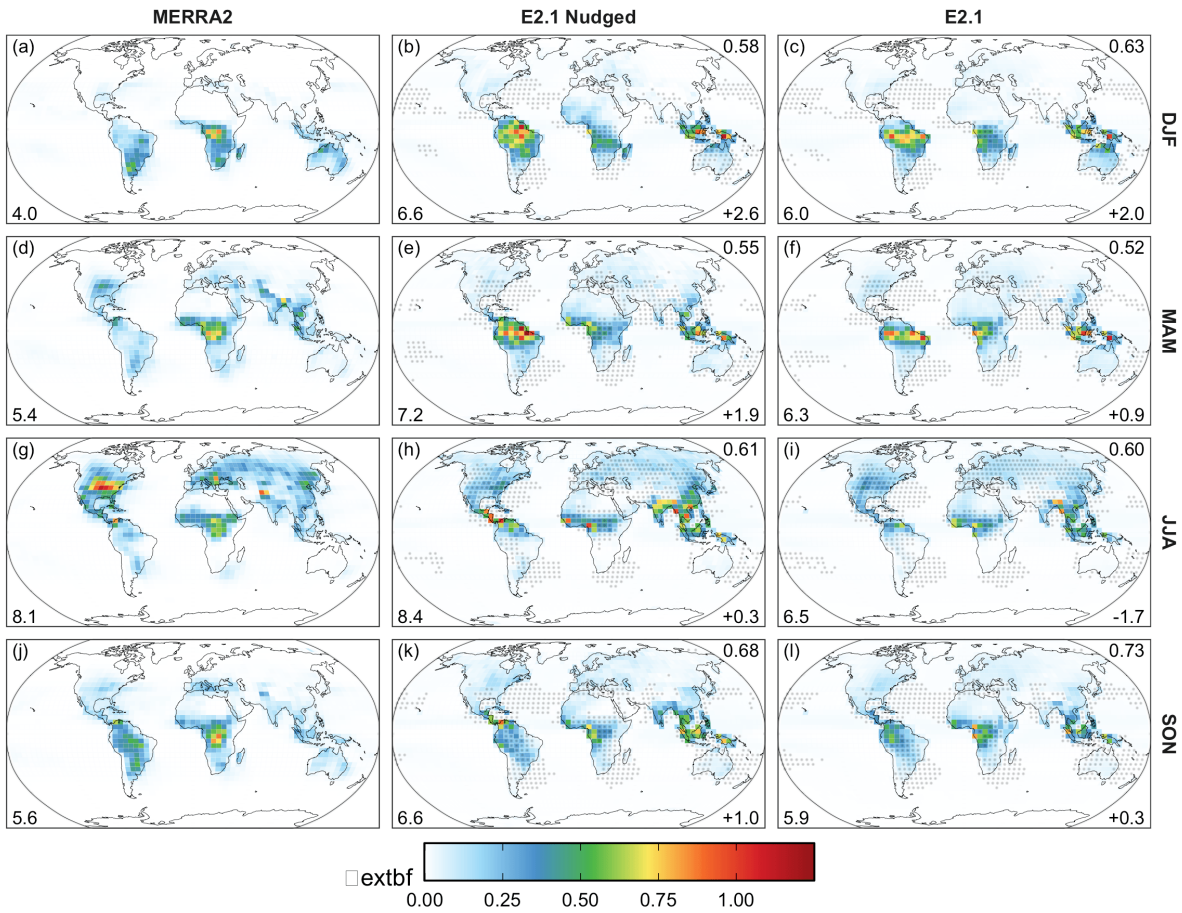

Figure S59: Same as **Fig. S55**, but for vertically integrated columns of NO from lightning, and with global total units of Tg N a^{-1}.

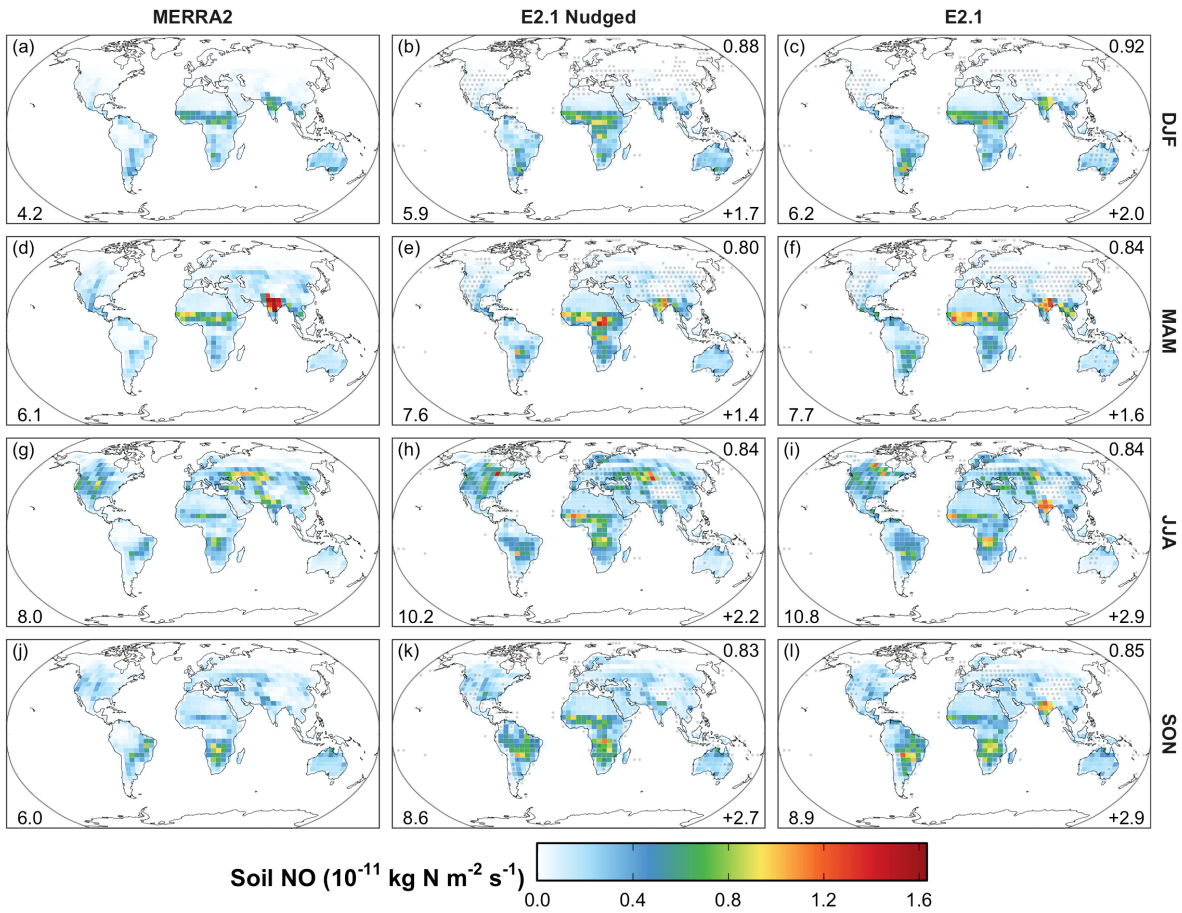

Figure S60: Same as **Fig. S59**, but for NO from soil microbial activity.

S3 Evaluation

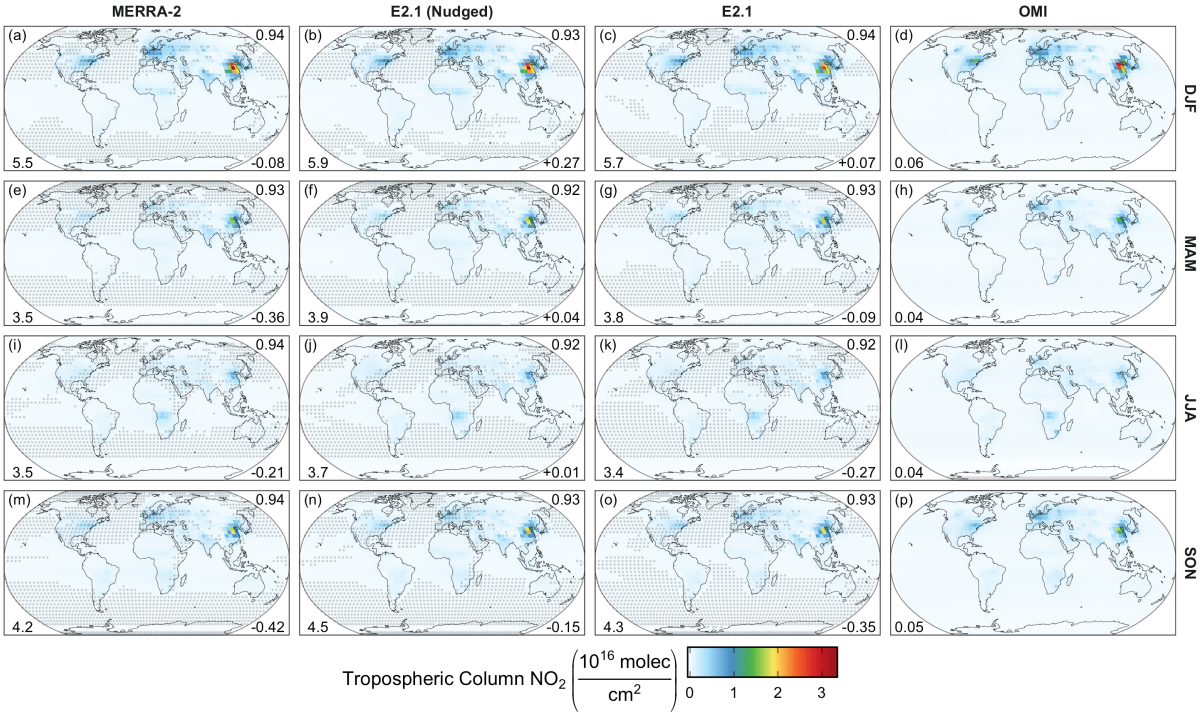

Figure S61: The same as panels a-d of Fig. 15 in the main text, but for each season.

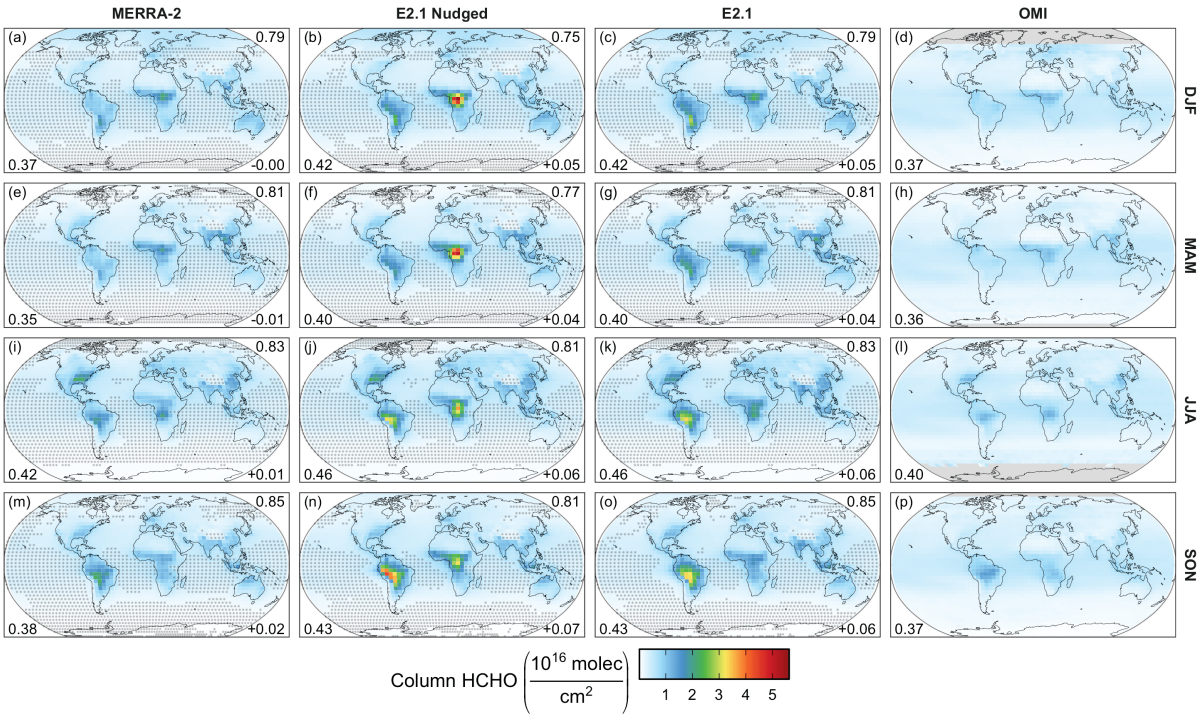

Figure S62: The same as panels e-h of Fig. 15 in the main text, but for each season.

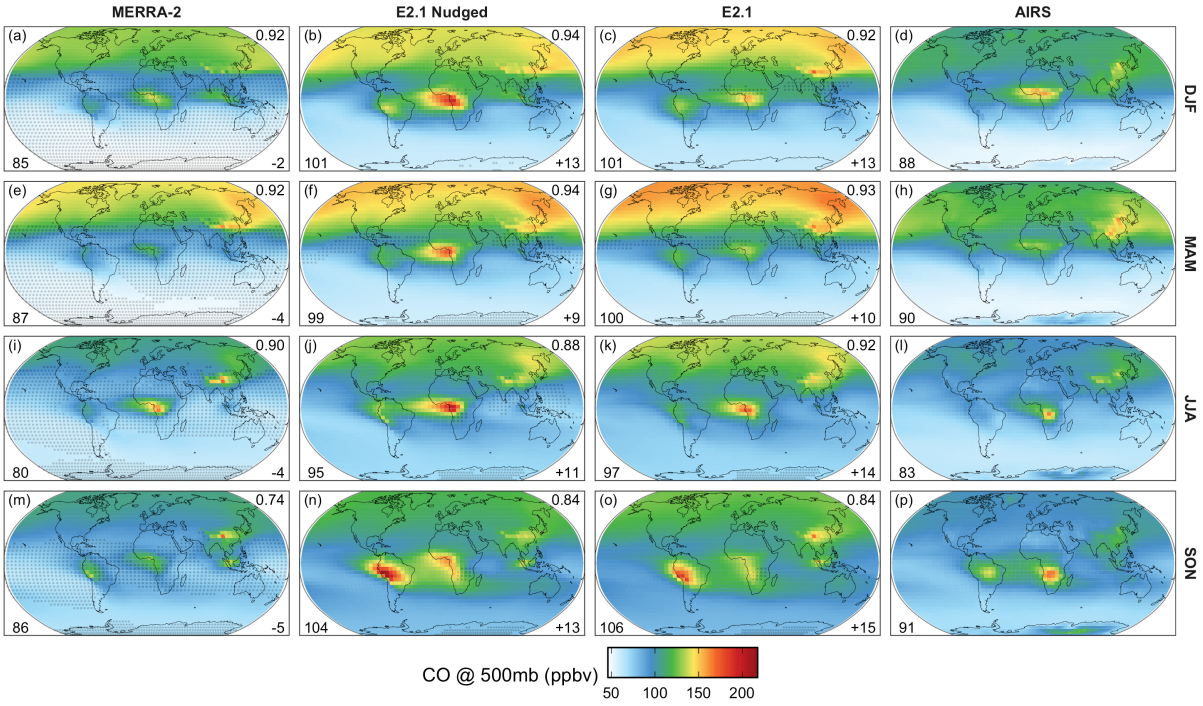

Figure S63: The same as panels i-l of Fig. 15 in the main text, but for each season.

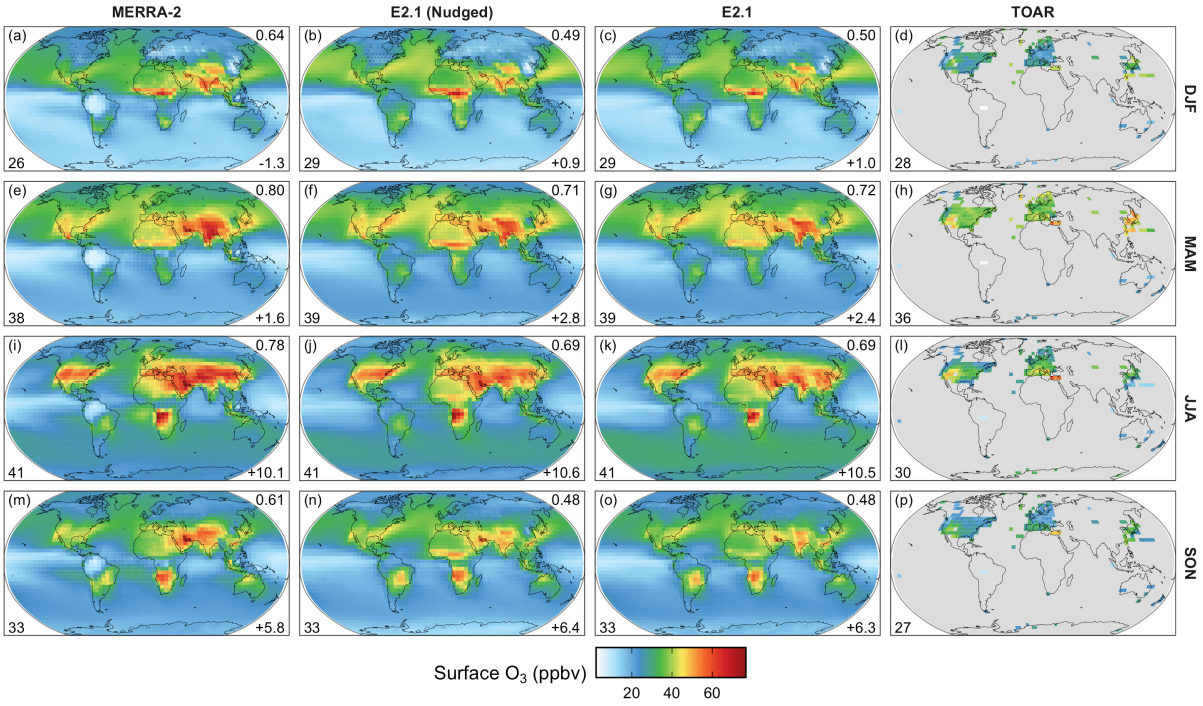

Figure S64: The same as panels a-d of Fig. 16 in the main text, but for each season.

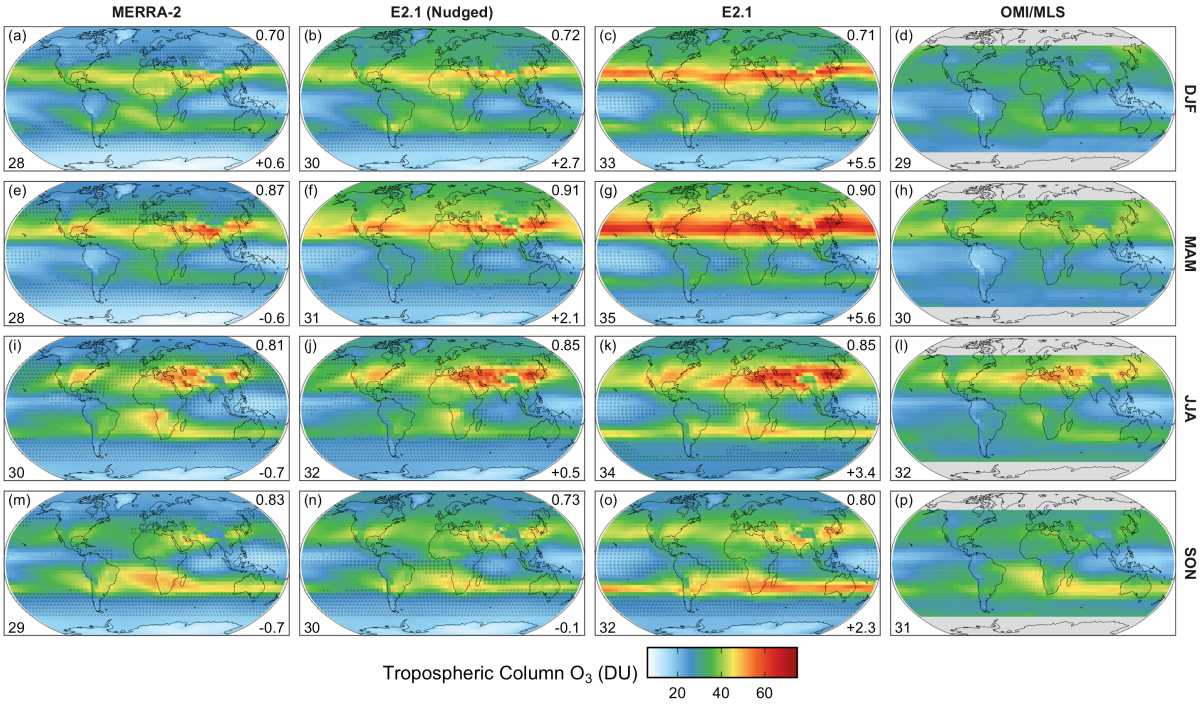

Figure S65: The same as panels e-h of Fig. 16 in the main text, but for each season.

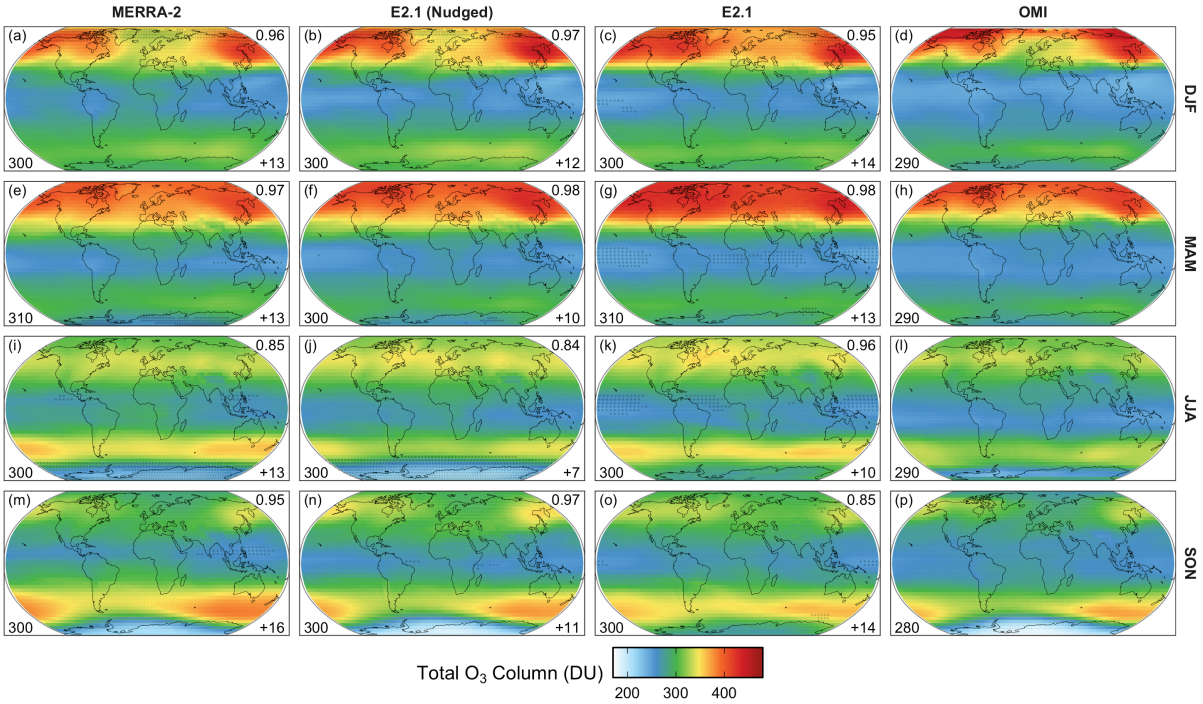

Figure S66: The same as panels i-l of Fig. 16 in the main text, but for each season.

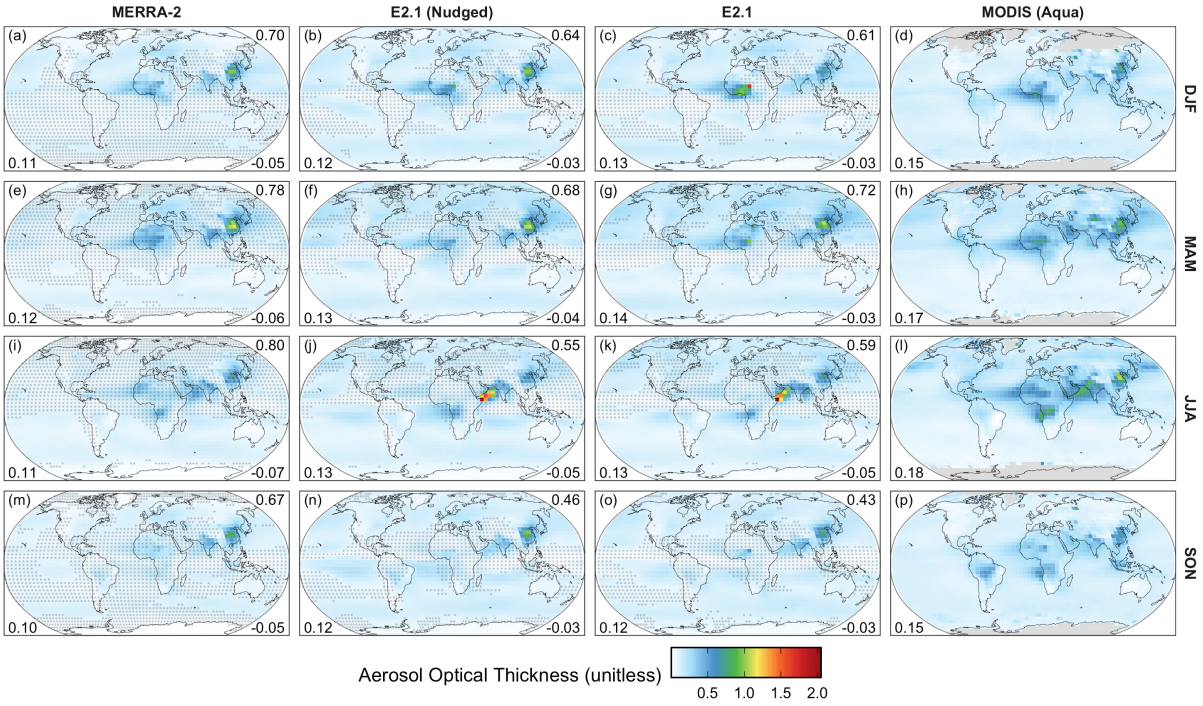

Figure S67: The same as panels e-h of Fig. 16 in the main text, but for each season.

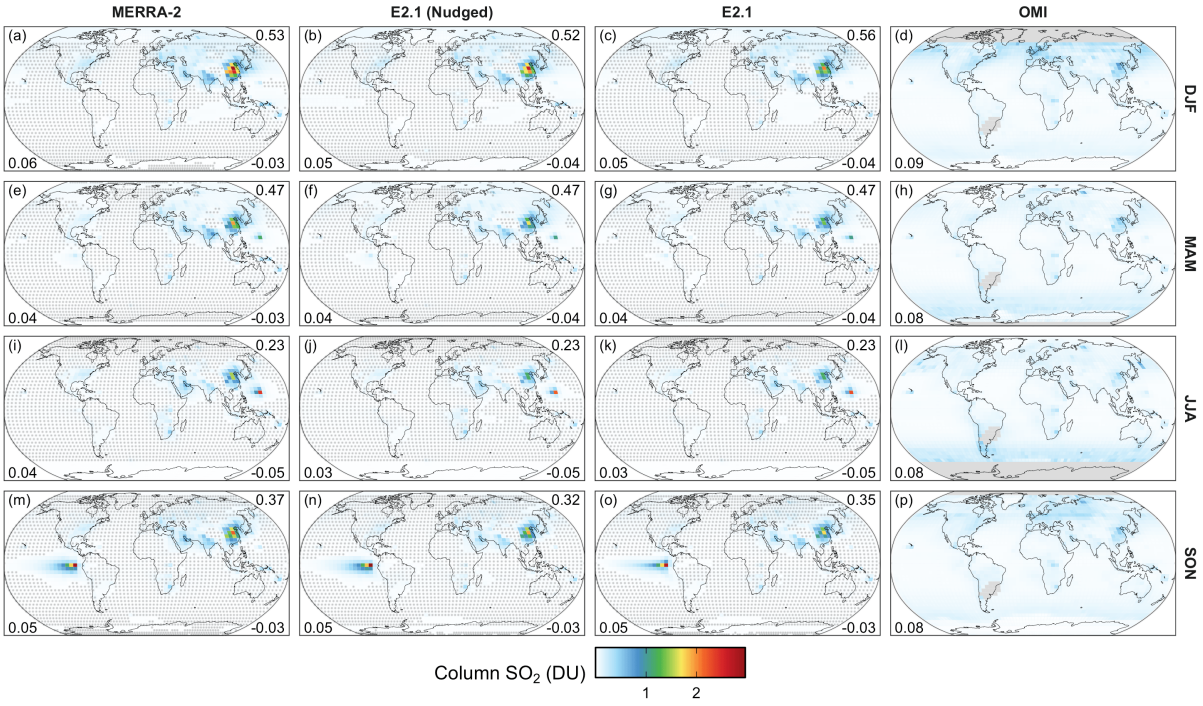

Figure S68: The same as panels i-l of Fig. 16 in the main text, but for each season.

References

Gelaro, R., McCarty, W., Suárez, M., Todling, R., Molod, A., Takacs, L., Randles, C., Darmenov, A., Bosilovich, M., Reichle, R., Wargan, K., Coy, L., Cullather, R., Draper, C., Akella, S., Buchard, V., Conaty, A., da Silva, A., Gu, W., Kim, G., Koster, R., Lucchesi, R., Merkova, D., Nielsen, J., Partyka, G., Pawson, S., Putman, W., Rienecker, M., Schubert, S., Sienkiewicz, M., and Zhao, B.: The Modern-Era Retrospective Analysis for Research and Applications, Version 2 (MERRA-2)., J Climate, Volume 30, 5419–5454, https://doi.org/10.1175/JCLI-D-16-0758.1, 2017.

Gidden, M. J., Riahi, K., Smith, S. J., Fujimori, S., Luderer, G., Kriegler, E., van Vuuren, D. P., van den Berg, M., Feng, L., Klein, D., Calvin, K., Doelman, J. C., Frank, S., Fricko, O., Harmsen, M., Hasegawa, T., Havlik, P., Hilaire, J., Hoesly, R., Horing, J., Popp, A., Stehfest, E., and Takahashi, K.: Global emissions pathways under different socioeconomic scenarios for use in CMIP6: a dataset of harmonized emissions trajectories through the end of the century, Geoscientific Model Development, 12, 1443–1475, https://doi.org/10.5194/gmd-12-1443-2019, 2019.

van Marle, M. J. E., Kloster, S., Magi, B. I., Marlon, J. R., Daniau, A.-L., Field, R. D., Arneth, A., Forrest, M., Hantson, S., Kehrwald, N. M., Knorr, W., Lasslop, G., Li, F., Mangeon, S., Yue, C., Kaiser, J. W., and van der Werf, G. R.: Historic global biomass burning emissions for CMIP6 (BB4CMIP) based on merging satellite observations with proxies and fire models (1750–2015), Geoscientific Model Development, 10, 3329–3357, https://doi.org/10.5194/gmd-10-3329-2017, 2017.